VIENNA
UNIVERSITY OF
TECHNOLOGY

INSTITUTE OF
PHOTOGRAMMETRY
AND REMOTE SENSING

DIPLOMARBEIT

Calibration-Related Artefacts in the initial ASCAT Soil Moisture Product

Ausgeführt zum Zwecke der Erlangung des akademischen Grades
eines Diplom-Ingenieur/in unter der Leitung von

Univ.Prof. Dipl.-Ing. Dr.techn. Wolfgang Wagner
Institut für Photogrammetrie und Fernerkundung

eingereicht an der Technischen Universität Wien
Fakultät für Mathematik und Geoinformation
von

Sebastian Hahn

Matrikelnummer 0525509
Obere Hauptstraße 34/9
A-2326 Lanzendorf

Wien, am 9. März 2011 .....

Abstract

Since December 2008 the European Organisation for the Exploitation of Meteorological Satellites (EUMETSAT) has been operationally distributing a global 25 km surface soil moisture product derived from the Advanced SCATterometer (ASCAT) on board the meteorological operational satellite METOP-A. Soil moisture is retrieved by using the change detection model originally developed for the Active Microwave Instrument (AMI) flown on the European satellites ERS-1 and ERS-2 by the Vienna University of Technology (TU-Wien). With the launch of the first of three METeorological Operational Platforms (METOP-A) in October 2006, ASCAT on board METOP-A inherits and continues the role of his predecessor AMI. The original soil moisture retrieval algorithm was expected to be almost directly applicable for ASCAT with only minor changes, since the configuration and technical design is similar to the ERS scatterometers. An important aspect for the TU-Wien model is to have a robust historic long-term reference data set of scattering parameters. In view of this fact, the initial ASCAT soil moisture product had to rely on the model parameters derived from over 15 years of ERS-1/2 data sets. Because of differences in calibration and resolution, the combination of ASCAT backscatter measurements and ERS-1/2 historic long-term reference causes some problems in the initial ASCAT soil moisture product.

The objective of the present master thesis was to analyse and investigate the initial ASCAT soil moisture product with the main focus on quantification of the impact from the ERS-1/2 historic long-term reference data set. Therefore, a model was developed to investigate the expected two main effects: spatial resolution and calibration difference. It turned out that a simple model is able to describe the remaining artefacts in the initial ASCAT soil moisture product due to a spatial resolution difference, which especially occur in areas characterized by sharp backscatter contrasts. The expected behaviour in case of different absolute calibration could have been modeled as well, though the characteristics are decreasing with increasing soil moisture.

Kurzfassung

Seit Dezember 2008 läuft der operationelle Vertrieb eines globalem 25 km Bodenfeuchte Produkts durch die Europäische Organisation für die Nutzung meteorologischer Satelliten (EUMETSAT), abgeleitet aus *Advanced Scatterometer* (ASCAT) Messungen an Bord des *meteorological operational satellite* METOP-A. Bodenfeuchte wird mit Hilfe eines von der Technischen Universität Wien (TU-Wien) entwickelten *change detection* Algorithmus gewonnen, welcher ursprünglich für das *Active Microwave Instrument* (AMI), an Board der beiden Europäischen Satelliten ERS-1 und ERS-2, entwickelt wurde. Mit dem Start der ersten von drei *METeorological Operational Platforms* (METOP-A) im Oktober 2006, übernimmt und verbessert ASCAT an Bord von METOP-A die Rolle seines Vorgängers AMI. Es war zu erwarten, dass der *soil moisture retrieval* Algorithmus nahezu unverändert auf ASCAT anwendbar sein würde, da die Konfiguration und das technische Design sehr ähnlich zu den ERS Scatterometern ist. Ein wichtiger Aspekt für das TU-Wien Modell ist jedoch ein robuster langzeit Referenzdatensatz von *scattering parameters*. In anbetracht dessen, musste sich das anfängliche ASCAT Bodenfeuchte Produkt auf Modellparameter, abgeleitet aus über 15 Jahren ERS-1/2 Datensätzen, beziehen. Allerdings aufgrund unterschiedlicher Kalibrierung und Auflösung verursacht diese Kombination aus ASCAT Messungen und der historischen Langzeitreferenz Probleme im anfänglichen ASCAT Bodenfeuchte Produkt.

Die Zielsetzung der Diplomarbeit ist daher die Analyse des anfänglichen ASCAT Bodenfeuchte Produkts, wobei der Schwerpunkt auf der Quantifizierung des Einflusses des ERS-1/2 historischen langzeit Referenzdatensatzes auf das Bodenfeuchteprodukt liegt. Demzufolge wurde ein Modell entwickelt, welches die beiden zu erwartenden Hauptursachen untersuchen soll: Unterschiede in räumlicher Auflösung und Kalibrierung. Es zeigte sich, dass ein simples Modell in der Lage ist die verbleibenden Artefakte aufgrund unterschiedlicher räumlicher Auflösung im anfänglichen ASCAT Bodenfeuchte Produkt zu beschreiben, welche speziell in Gebieten mit scharfen *backscatter* Kontrasten auftraten. Das zu erwartende Verhalten im Falle von absoluter Kalibrierungsunterschiede konnte ebenfalls erfolgreich simuliert werden, allerdings nimmt diese Charakteristik mit zunehmender Bodenfechte ab.

Acknowledgments

The present research was accomplished at the Institute of Photogrammetry and Remote Sensing (IPF), Vienna University of Technology. It was a pleasure performing my Master Thesis in such a great research environment. I would like to thank all those who contributed to this study. Special thanks goes to my supervisor Professor Wolfgang Wagner, who gave me the chance to expand my experience in remote sensing, as well as the possibility to work in a professional and motivated team. His regular guidance and excellent expertise was a great support and motivation for the composition of this piece of work.

Many thanks to all my colleagues at IPF, especially: Stefan Hasenauer, Vahid Naeimi, Daniel Sabel, Marcela Doubkova, Christoph Paulik and Hans Thüminger. Their suggestions, discussions and technical assistance were marvelous offering me new perspectives and possibilities. Special thanks in this respect goes to Richard Kidd, who always reinforced my self-confidence, as well as Zoltan Bartalis, with his excellent knowledge.

I would like to thank my family for their continuous encouragement during my education, but especially my fiancée Yvonne Ivanics for her patience and care all the time. Last but not least, I want to thank our Australian Shepherd Luis, who tried to keep me fit those days and donated me valuably breaks with a lot of fresh air.

Contents

List of Figures vii

List of Tables ix

List of Acronyms x

1 Introduction 1

1.1 The initial ASCAT Soil Moisture Product . . . 2
1.2 Study Approach . . . 6
1.3 Objective and Structure of Work . . . 6

2 Spaceborne Scatterometry 8

2.1 Measurement Principle . . . 10
2.1.1 The radar equation . . . 11
2.1.2 Resolution . . . 15
2.1.3 Calibration . . . 18
2.2 ASCAT on board METOP-A . . . 19
2.2.1 Instrument description . . . 21
2.2.2 Geometry and coverage . . . 22
2.2.3 Product processing . . . 24

3 Soil moisture retrieval at the Vienna University of Technology 27

3.1 TU-Wien Soil Moisture Retrieval Method . . . 28
3.1.1 Normalisation . . . 29
3.1.2 Vegetation correction . . . 33
3.1.3 Surface soil moisture retrieval . . . 34
3.2 WAter and Retrieval Package (WARP) . . . 38
3.2.1 WARP 5.2 . . . 40
3.2.2 WARP NRT . . . 44

4 Characterisation of calibration-related soil moisture artefacts **48**
4.1 Modelling consequences of calibration-related conflicts 49
4.2 Splitting resolution- and absolute calibration-related effects 51
4.3 Availability of model parameters 51

5 Results and Discussion **53**
5.1 Model considerations and characteristics 53
5.2 Simulating calibration-related artefacts 55
5.3 Consequences of the resolution mismatch 59
5.4 Impact of absolute calibration differences 62
5.5 Comparison to soil moisture noise 67

6 Summary and Outlook **69**

Bibliography **71**

List of Figures

1.1 The initial ASCAT surface soil moisture product 5

2.1 Basic elements of a radar system 11
2.2 Basic geometry of a bistatic radar 12
2.3 Geometry of a side-looking real aperture radar 15
2.4 METOP-A payload 20
2.5 Daily coverage ERS-1/2 and METOP-A 22
2.6 Measurement geometry of METOP-A ASCAT 23
2.7 Overview of ASCAT Level 1 products 25

3.1 Backscatter behaviour for different biomes 30
3.2 Incidence angle dependency of backscatter due to soil moisture or vegetation change 31
3.3 Calculation of local slope and an example of linear fitting through local slope values 32
3.4 Crossover angle concept 33
3.5 An example of $\sigma^0(40°)$ time series at a location near Salamanca, Spain 35
3.6 Wet backscatter reference, lowest dry backscatter reference and sensitivity derived from ASCAT 36
3.7 Wet correction and sensitivity after correction 37
3.8 WARP 5.2 flowchart 42
3.9 Offline soil moisture processing chain implemented at TU-Wien 43
3.10 WARP NRT flowchart 45
3.11 Online soil moisture processing chain implemented at EUMETSAT 47

5.1 Equation (5.1) in a graphical manner 54
5.2 Statistics derived from the deviations originated by all calibration-related differences 56
5.3 Global maps illustrating the total calibration-related modeled deviations 57

5.4 A closer look on Europe and North Africa showing the deviations coming from the total calibration-related mismatch 58
5.5 Statistics derived from deviations arising by a resolution mismatch 59
5.6 Simulated deviations as a consequence of a resolution mismatch on global maps 60
5.7 A closer look on Europe and North Africa showing the deviations arising by a resolution mismatch 61
5.8 Statistics derived from simulated deviations arising by an absolute-calibration difference 62
5.9 Simulated deviations as a consequence of an absolute calibration difference on global maps 63
5.10 A closer look on Europe and North Africa showing the deviations coming from an absolute calibration difference 64
5.11 The impact on soil moisture with a simulated bias of 0.22 dB 65
5.12 Simulated deviations due to an absolute calibration difference for dry conditions in Argentina, South America 66
5.13 Vegetation index anomaly derived from MODIS on NASA's Terra satellite for January 17 - February 1, 2009 66
5.14 Maximum soil moisture noise 67
5.15 A comparison of the simulated deviations to the maximum soil moisture noise 68

6.1 The initial ASCAT soil moisture product processed with current ERS-1/2 model parameters and first results with updated model parameters based on 2 years of ASCAT 70

List of Tables

2.1 Past, present, and planned scatterometer missions 10

3.1 Comparison between WARP and WARP NRT. 39

4.1 Available model parameters 52

List of Acronyms

ASCAT	Advanced Scatterometer on board METOP-A
DGG	Discrete Global Grid
ECMWF	European Centre for Medium-Range Weather Forecasts
EPS	EUMETSAT Polar System
ERS	European Remote Sensing Satellite (ESA)
ESA	European Space Agency
ESD	Estimated Standard Deviation
EUMETSAT	European Organisation for the Exploitation of Meteorological Satellites
GMF	Geophysical Model Function
IPF	Institute of Photogrammetry and Remote Sensing, Vienna University of Technology
KNMI	Royal Netherlands Meteorological Institute
METOP	Meteorological Operational Satellite (EUMETSAT)
NRT	Near real-time
NWP	Numerical Weather Prediction
NWP SAF	Satellite Application Facility on Numerical Weather Prediction
RCS	Radar Cross-Section
SAF	Satellite Application Facility (EUMETSAT)
SAR	Synthetic Aperture Radar
SASS	Seasat-A Scatterometer System
WARP	Water Retrieval Package (IPF)
WMO	World Meteorological Organization

Chapter 1

Introduction

Like all biological life-forms, also products may go through similar stages during their “life”. Such a concept is often used in business management and marketing to describe the entire life cycle of consumer products from its conception and design, through manufacture and service, to decline and disposal (*Stark*, 2005). In general, a product life cycle is characterised by multiple phases and involves many disciplines. Very often the four main stages of a product’s life cycle are specified as: birth, growth, maturity and decline. Of course, such a concept may be questionable in case of products derived from instruments carried by satellites, but if someone takes a closer look similarities can be found. Although earth observation is a technically domain, marketing and management are crucial points if a mission will be approved or not.

In many cases the user community plays a decisive role, which satellite products are of more casual interest or dispensable. But also new ideas or technologies are determining factors. At this point a preliminary assessment of the project management is ostensible and will result into a specification of the mission concept. This stage is often followed by a feasibility study to identify constraints and quantify critical elements. The subsequent phase deals with a preliminary definition of the project and products, as well as the confirmation of the feasibility related to the recommended solution. A detailed study and definition of the chosen solution will end up in a critical design review together with a first prototype, which can be tested against the system requirements. The last step encompass the realisation and maintenance of the whole system. The spacecraft needs to be carried into the chosen orbit, whereby all instruments require a check-up in space and if necessary a recalibration. After everything is working steadily, the first products can be computed and delivered to the user community. It is worth to note that the satellite life time is controlling the product life time as well, since without any additional measurements the product generation can be closed. Thus, only subsequent missions will allow to continue the product (*Wertz and Larson*, 1999).

This general attempt to formulate a satellite's product life cycle, which is actually linked to a project life cycle, already points out its analogy to the concept mentioned in the beginning. Many different disciplines work together at different stages of development, at which the product can prosper. Of course, some phases differ completely and may go beyond typical product life stages, but the overall path is actually similar at a different framework.

Products may also arise in a later phase, for example during the mission commissioning phase. Thereby, first measurements help to develop a new model or insights, which in turn allow to derive a new quantity whose physical relationship was so far unknown or not accurately understood. Or again user requests are the trigger for new products formulated in a later phase of the mission. If it is possible to design a model in such a way that is more related to the instrument itself then to the whole mission, the new product will give a higher durability in the future. This is because only the instrument needs to be a payload on another mission and a cloning of the previous mission parameters is not necessary.

A model which showed such transfer capabilities is the soil moisture retrieval algorithm introduced by *Wagner et al.* (1999a). It was first developed for the Active Microwave Instrument (AMI) flown on the European Remote Sensing Satellites ERS-1 and -2. Now it is adapted to the Advanced Scatterometer (ASCAT) on board METOP-A. However, in terms of a product life cycle it is still in its initial state, since an update of essential model parameters is still pending.

1.1 The initial ASCAT Soil Moisture Product

On 19 October 2006 the first of a series of three Meteorological Operational satellites (METOP-A) was launched from Baikonur Cosmodrome, which is located in the desert steppes of Kazakhstan. This meteorological platform carries the Advanced Scatterometer ASCAT, which is a real aperture radar operating in C-band with vertical polarization (VV). The instrument was predominantly designed to measure wind speed and direction over the ocean. However, measurements from ASCAT will also find its application in a number of other areas such as monitoring of land- and sea-ice, snow cover and soil moisture (*Figa-Saldaña et al.*, 2002).

At its 17th meeting in 2004, the Science Working Group (SWG) of the Science and Technical Group (STG) of the European Organisation for the Exploitation of Meteorological Satellites (EUMETSAT) determined the need for an operational global soil moisture product, especially for Numerical Weather Prediction (NWP). This decision, based on a specific user request, devised soil moisture to be an operational, so-called *Day 2 product*, from ASCAT on board the first METOP satellite. In general, day 2 products are not specified in the beginning of the original system requirements and are usually added after completion of the commissioning phase of the instrument (*Klaes et al.*, 2007). EUMETSAT was tasked to identify the feasibility with

respect to the NWP requirements. A user requirement study realised by the Vienna University of Technology on behalf of EUMETSAT and the NWP Satellite Application Facility (NWP SAF) collected and identified the common needs for a global soil moisture product (*Kidd*, 2005). In addition, an implementation plan was developed in order to show the technical feasibility (*Wagner*, 2005). In 2007 the first prototype was ready and delivered to EUMETSAT. The so-called WARP NRT processor was directly installed at EUMETSAT's Central Application Facility (CAF) in Darmstadt, Germany. Since the prototype was written in the programming language IDL and EUMETSAT uses C++, the whole prototype needs to be transformed and adapted to the new system environment. No major problems occurred during the first trial dissemination, which started in May 2008. Thus, the operational ASCAT surface soil moisture product could be officially released in December 2008 (*EUMETSAT*, 2008).

Previous to the online WARP NRT processor used at EUMETSAT, the Vienna University of Technology has developed an offline processing tool for soil moisture retrieval as well, called WAter and Retrieval Package (WARP). The term *offline* should indicate that the product generated by WARP will only be infrequently updated and extended, whereas the *online* processor, WARP NRT, will deliver soil moisture in near real time. Behind both processors is the same algorithm, but with the difference that WARP is a comprehensive and complex software tool, whereas WARP NRT is a rather small processing chain. This is due to the fact that WARP NRT should perform a very fast and robust computation of soil moisture. It therefore requires also predefined look-up tables and model parameters. The model parameters are essential co-products in the offline processor WARP, which consists scattering characteristics for discrete grid points on the land surface of the Earth. The concept of WARP is a modular structure that follows major processing steps in order to derive the different model parameters gradually and finally relative surface soil moisture.

The soil moisture retrieval underlying the online as well as the offline processor is based on the method initially presented by *Wagner et al.* (1999a). This approach together with a recent update from *Naeimi* (2009) constitute the current version of the soil moisture retrieval method. The update in the latest offline version WARP 5.2 include an error model, improvements in the model parameter computation, as well as the possibility to migrate the soil moisture retrieval from ERS-1/2 to METOP-A scatterometer data. The latest version of the WARP NRT processor is 2.0, which still uses model parameters derived from 50 km ERS-1/2 datasets (01/1992-01/2001 and 08/2003-05/2007). However, this yields to a spatial resolution mismatch between the ASCAT σ^0 measurements at 25 km resolution compared to the ERS-1/2 model parameters, which are only available in 50 km resolution. In addition, both ASCAT soil moisture products (the higher resolution and the nominal resolution) suffer from possible presence of inter-calibration biases between the σ^0 measurements from ERS-1/2 and

METOP-A scatterometer, as well as the not entirely overlapping incidence angle range of the two instruments. Thus, to counteract at least against the absolute calibration bias, a bias correction provided by the Royal Netherlands Meteorological Institute (KNMI) were used.

Anyhow, it was considered to update the model parameters once enough ERS-2 data were reprocessed to a higher resolution (25 km) and a new model parameter database could be computed based on ASCAT and ERS-2 data in the offline regime. This merging would subsequently account for the calibration-related discrepancy. But since ESA has not completely reprocessed the ERS-2 data so far, the mixture of ERS-1/2 model parameters together with METOP-A scatterometer measurements is still ongoing.

A merging between ERS and METOP-A scatterometer data would of course require a backscatter analysis in order to establish a common Level 1 calibration of both instruments. First analysis pointed out that a cross-calibration between ASCAT and the ERS scatterometers is not trivial. The collocation study presented in *Bartalis* (2009), for the period 2007-2008, showed that at least for the common incidence angle range, the ASCAT σ^0 measurements are on average approximately 0.22 dB higher then those of ERS-2. It is also mentioned that ASCAT soil moisture values show a pronounced decrease towards the higher end of incidence angles, which would mean a bias with respect to the incidence angle. Thus, normalisation corrections based on the outcome of this collocation study would indeed reduce the absolute bias in soil moisture, but fail to account for the incidence angle bias.

To sum up, the current status of the operational ASCAT soil moisture product is that it is still situated in its initial state, since the model parameters have not been updated so far. Figure 1.1 shows the initial ASCAT soil moisture product over Central Europa in both resolutions, research (25 km) and nominal (50 km), respectively. Artefacts are clearly visible due to the resolution mismatch, especially in areas with a high backscatter contrast (e.g. around cities). Due to the assumption that this initial state will not last for such a long time, a quantitative analysis of the calibration-related mixture has not been investigated so far.

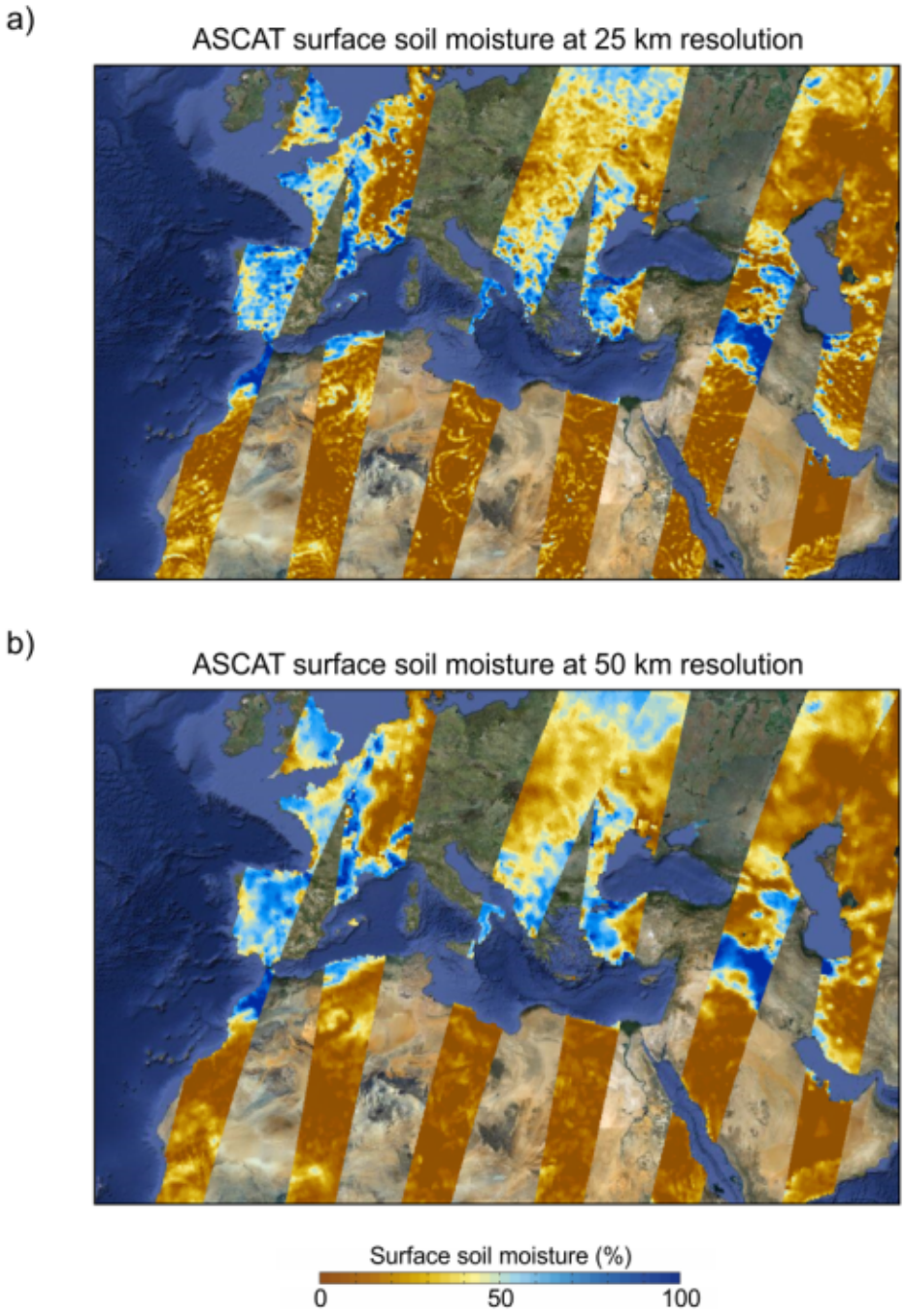

Figure 1.1: The initial ASCAT surface soil moisture product in 25 *km (a) and* 50 *km (b) resolution. Both images show the soil moisture conditions from 2011/01/30 over Europe and North Africa overlayed on Google satellite images.*

1.2 Study Approach

There are several ways to investigate the impact of this calibration-related mismatch. One might be a direct comparison between the offline and online soil moisture products, but this will not allow to separate the different effects and investigate their individual magnitude. Another approach could be to estimate the consequence of every processing step within the model parameter derivation, which may lead to a complex formulation probably rising more questions then giving answers. A further imaginable starting point could be running the whole offline soil moisture retrieval again with a known synthetic bias in the measurements and with different spatial resolutions. Unfortunately the processing time take several weeks for one test run, which disqualifies this solution and makes it impracticable.

A parametrisation of the last equation in the soil moisture retrieval allows to split the different effects, as well as determining their magnitude. It is a quite simple approach, but with the possibility to model also the impact of different soil moisture conditions. Therefore this approach seems to be best suited to investigate the problem. The derivation of this model will be treated within chapter 4, whereas the results are shown in the subsequent chapter 5.

1.3 Objective and Structure of Work

In general, the initiation of a model based on different datasets requires in the beginning a homogenisation between them. A mismatch could have many reasons (e.g. spatial-, temporal resolution, measured variable, absolute calibration, sensor geometry, etc.), but only after an exploration of the discrepancies and the consideration of an unification it is possible to use all datasets together.

In case of the initial ASCAT soil moisture product a loss of quality was excepted due to a spatial resolution, as well as an absolute calibration mismatch between the METOP-A ASCAT backscatter measurements and the model parameters derived from ERS-1/2 scatterometers. In the first place this was planned as an intermediate solution, as long as there are not enough ASCAT measurements and the ERS-2 data is not available at 25 km resolution. Thus, it was not considered to investigate the impact of this mixture, but to minimise at least the absolute calibration difference within the processing with bias corrections. However, ERS-2 data has not been reprocessed to higher resolution completely so far and the solution described above is still active since two years.

The presented study is motivated by the desire to learn from this ongoing situation and to design a model which allows to quantify the impact of the calibration mixture on the soil moisture values. The major questions are, which regions are mostly affected and where does

the dominant cause come from. Moreover, if the model will be able to split up different effects and how these results will compare to the estimated soil moisture noise from the error model. This would give an information about the quality of the initial ASCAT soil moisture product, as well as the possibility to learn more about model parameters based on different datasets.

The presented work is structured as follows: **Chapter** 1 already started with a brief introduction about the current status of the initial ASCAT Soil Moisture Product and an idea about the way of investigating the problem. The measurement principle of spaceborne scatterometry and a short history review will be covered by **Chapter** 2. The instrument design of ASCAT on board METOP-A will also be shortly presented in the same chapter. An elaborate summary about the soil moisture retrieval at the Vienna University of Technology, as well as the implementation of the algorithm is included in **Chapter** 3. The subsequent **Chapter** 4 deals with the derivation of the model used to simulate the calibration-related artefacts, which are still visible in the initial ASCAT soil moisture product. A detailed discussion on the outcome of the model will be presented in **Chapter** 5. Finally, the study will be completed with an overall summary, recommendations and an outlook in the last **Chapter** 6

Chapter 2

Spaceborne Scatterometry

A scatterometer is an active microwave instrument that transmits electromagnetic pulses and measures the energy scattered back. They are designed to measure at a particular angle, frequency and polarisation, but most of the existing instruments measure over a range of one or more of these parameters. The normalized radar cross section σ^0 is the quantitative description of the received energy at the instrument. The intensity depends mostly on the roughness and dielectric properties of the illuminated target. Spaceborne scatterometer are so-called *non-imaging* or *real-aperture* radar systems, which indicates a lower spatial resolution compared to the SAR technique (*synthetic-aperture radar* or *imaging radar*) or the spatial resolution that one might be familiar with from optical remote sensing.

The direction of the antennae is usually on one side only to avoid ambiguities of the received signal. A result of the *side-looking geometry* is that the measured backscattering coefficients σ^0 are arranged in a swath aligned to the flight direction of the instrument carrier. The footprint size generated by one antenna is mainly dependent on the construction design. For example, a relatively small spot-like pattern can be produced with a parabolic dish antenna ("pencial beam") or a long drawn-out but very small beam by using a rectangular antenna ("fan-beam").

One of the first applications of scatterometry has been near-surface winds over the ocean. During the World War II the development of the radar technology was sped up because of the attempt to detect hostile objects such as planes or ships. The received signals over open sea were very noisy and the radar operators at that time called this phenomenon "sea clutter". Only later it has been realised that this clutter came from sea wave crests, which contribute to the radar signal. Nowadays this effect is utilised by combining measurements of different azimuth angles and putting them into a geophysical model function (GMF), which relates wind and backscatter. The result is a near-surface wind vector field over the ocean, which can be used in numerical weather prediction (NWP) or monitoring of hurricanes.

Scatterometer experiments in space started in 1973 with the instrument S-193 RADSCAT on board NASA's Skylab space station (*Jordan et al.*, 1976; *Ross and Jones*, 1978). The sensor was a combination between a radiometer and scatterometer working in the Ku-Band at 13.9 GHz. The first operational scatterometer in space was known as SASS (Seasat-A Scatterometer System) on board the satellite Seasat launched in June 1978 (*Born et al.*, 1979). It was designed for remote sensing of the earth's oceans to collect data on sea-surface winds, sea-surface temperatures, wave heights and oceanic topography (*Grantham et al.*, 1977). Unfortunately the mission ended after only 104-days due to a malfunction. It was temporarily silent in the spaceborne scatterometery domain until the nineties, when the European Space Agency (ESA) started their first Earth Remote Sensing Satellite (ERS-1) in July 1991. ERS-1 failed in March 2000, far exceeding its expected lifespan, gathering a lot of data, especially in the microwave domain. It's successor ERS-2 started in April 1995, which allowed a tandem mission phase with its predecessor (*Duchossois and Martin*, 1995; *Duchossois et al.*, 1996). Unfortunately, in 2001 ERS-2 suffered from the failure of several on board gyro systems, followed by a tape recorder male function in 2003. This led to only real time data download from ground stations in the line of sight and inventing an innovative new scheme, called Zero-Gyro Mode (ZGM), for flying and controlling the satellite without gyros (*Neyt et al.*, 2002; *Sunda et al.*, 2002). The satellite is now more than 14 years in space and was "operating nominally" in 2010, although its nominal mission life was planned to be only 3 years. The mission extension was approved to the end of 2011 (*CEOS*, 2010). Other spaceborne scatterometer launched within the last two decades were: the NASA Scatterometer (NSCAT) instrument on board ADEOS in 1996 (*Naderi et al.*, 1991), as well as the SeaWinds sensor on board two platforms, the American QuikSCAT in 1999 (*Tsai et al.*, 2000) and the Japanese ADEOS-II in 2003, respectively. One of the most recent mission with a scatterometer on board, is the METeorological Operational Platform (METOP-A) carrying the Advanced SCATterometer (ASCAT) launched in 2006 (*Figa-Saldaña et al.*, 2002).

The table (2.1) should give a short summary about the past, present and planned space missions with a scatterometer on board.

Platform	Instrument	Band	Spatial Res (km)	Launch	Status
Skylab	S-193	Ku	16	1973/05	over
Seasat	SASS	Ku	50	1978/06	over
ERS-1	AMI	C	50	1991/07	over
ERS-2	AMI	C	50	1995/04	operational
ADEOS	NSCAT	Ku	25,50	1996/04	over
QuikSCAT	SeaWinds	Ku	25	1999/06	operational
ADEOS-II	SeaWinds	Ku	50	2002/12	over
METOP-A	ASCAT	C	25,50	2006/10	operational
OCEANSAT-2	SCAT	Ku	50	2009/09	operational
HY-2A	SCAT	Ku	50	2011/01	planned
SAC-D	Aquarius	L	100	2011/04	approved
METOP-B	ASCAT	C	25,50	2012/04	approved
Meteor-M N3	Scatterometer	C (or X)	25	2012/12	approved
OCEANSAT-3	SCAT	Ku	50	2014/01	considered
Meteor-MP N1	Scatterometer	C (or X)	25	2014/12	planned
Meteor-MP N2	Scatterometer	C (or X)	25	2015/12	planned
METOP-C	ASCAT	C	25,50	2016/04	approved
Meteor-MP N3	Scatterometer	C (or X)	25	2016/12	planned

Table 2.1: Past, present, and planned scatterometer missions (Kramer, 2002; CEOS, 2010).

2.1 Measurement Principle

The basic elements of a *radar* (RAdio Detection And Ranging) are illustrated in Figure (2.1). It consists of a transmitter, which is used to produce electromagnetic waves and coupled into space through a transmitting antenna, together with a receiver antenna, which in turn feed the receiver circuits with the measured energy scatterd back by a conductive surface. After amplification at the receiver the signal can be further processed, in order to use some kind of indicator to extract information. A correlation between the transmitter and indicator allows a comparison of the transmitted and received signal characteristics. If the same antenna is used for both, transmission and reception, a so called transmit-receive switch (TR switch) is necessary to alternate between the two roles: transmitter and receiver.

In general, if an object is hit by an electromagnetic wave and the backscattered energy can be detected at the place of origin, the position of the object can be expected to be in the direction of wave propagation. The electromagnetic energy travels constantly with approximately the speed of light, which in turn can be used for determination of the distance by runtime measurements. Normally, the energy travels like a straight line through the space and will be affected only slightly due to the atmosphere and weather conditions. Thus, a focused radiation can be used to measure the direction of an object.

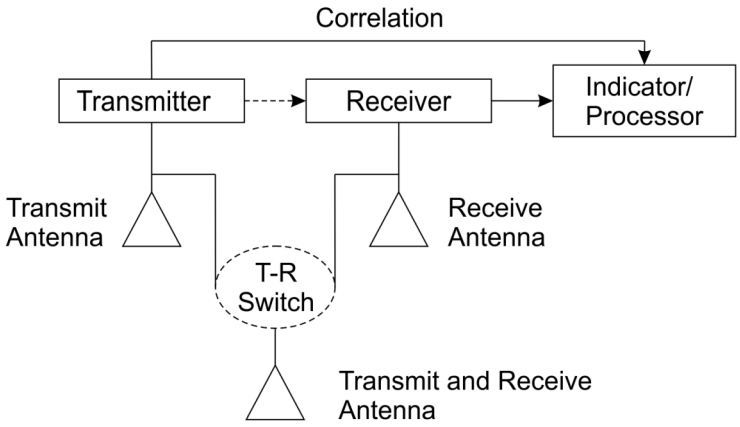

Figure 2.1: Basic elements of a radar system (after Ulaby et al. (1981)).

If a radar system allows to measure backscatter or reflectance properties of a surface quantitatively, it is called a scatterometer (*Ulaby et al.*, 1982). The received energy from the illuminated object depends on it's backscatter properties and can be expressed using the radar equation. The overall intensity of backscatter will be determined by the dielectric properties of the scattering medium. There is also an incidence angle dependent part, which is primarily governed by the surface geometry. A scatterometer which can be operated in such a way to obtain the backscatter coefficient σ^0 as a function of the incidence angle θ, often allows the identification of the surface type or its physical properties. In principle there are three methods to achieve this. The first one is to use a narrow-beamwidth in order to steer to a certain point in the target area. The second method is to use a Doppler processing of the received signal, since the frequencies are shifted slightly. The third method is to scan a range of incidence angles with very short pulses, which in turn can be uniquely allocated by resolving the time-structure of the returned pulse. The ability of resolving the incidence angle is equivalent to the spatial resolution.

2.1.1 The radar equation

The radar equation relates the system parameters (wavelength, polarization, resolution), measurement geometry (look angle, look direction) and target scattering properties (surface roughness, complex dielectric, slope angle, orientation) in a mathematical formulation in order to determine the returned energy (*Ulaby et al.*, 1982; *Henderson and Lewis*, 1998; *Woodhouse*, 2006). The presented radar equation is simplistic, since polarization effects are not included and it is confined to surface scattering. Figure 2.2 shows a schematically illustration of an antenna transmitting microwave radiation towards the surface.

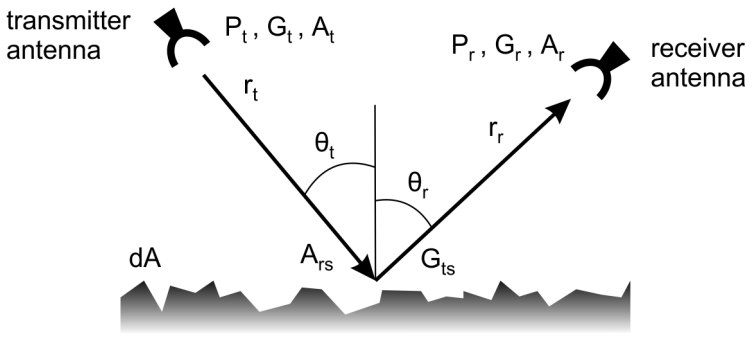

Figure 2.2: Basic geometry of a bistatic radar (after Ulaby et al. (1982)).

If the energy is transmitted in all directions (isotropically) into space the power density (power per unit area) is defined as the power transmitted P_t divided by the surface area of a sphere with a radius equal to the range distance (r) surrounding the antenna (spreading loss):

$$\text{Power density at range } r = \frac{P_t}{4\pi r^2} \qquad \left(\frac{W}{m^2}\right). \tag{2.1}$$

This equation describes the power density transmitted by a point source in all directions. However, normally directional antennas were used instead of isotropic ones. Thus, the power density will be increased by concentrating the energy into a certain direction, which is referred to as the gain of the transmitting antenna (G_t). The power density at the target in a distance r_t is now defined as:

$$\text{Power density at target} = \frac{P_t G_t}{4\pi r_t^2} \qquad \left(\frac{W}{m^2}\right). \tag{2.2}$$

Once the electromagnetic waves meet the target, the next parameter to be considered is the target. The total amount of the intercepted power by the target is proportional to the effective receiving area of the target (A_{rs}). Unless the target is a perfect conductor or a perfect insulator, some of the incident energy is absorbed (f_a) whereas the rest is reflected isotropically ($1 - f_a$). The attitude of the target is now comparable to a transmitter radiating the energy in a distinct pattern. Thus, the pattern may also have a certain gain (G_{ts}) towards the receiving antenna. The discussed parameters are usually combined into a single parameter called the radar cross section (RCS):

$$\sigma = A_{rs}(1 - f_a)G_{ts} \qquad (m^2). \tag{2.3}$$

Consequently, the radar cross section σ depends on the shape and dielectric properties, as well as the incident wave and the reradiated wave toward the receiver. The backscattered energy must travel from the target to the receiver (r_r), in order to be detect. This cause again an attenuation by a spreading loss of $1/4\pi r_r^2$. The effective aperture or receiving area of the antenna (A_r) is also decisive of how much energy can be detected. In the end, the total power received at the sensor (P_r) is the result of putting all these aspects together:

$$P_r = P_t G_t \left(\frac{1}{4\pi r_t^2}\right) \cdot A_{rs}(1-f_a) G_{ts} \cdot \left(\frac{1}{4\pi r_r^2}\right) A_r \qquad (W)\,. \tag{2.4}$$

Rearranging the equation (2.4) and using the radar cross section for substitution gives the final simple form of the so-called *bistatic radar equation*, since loss factors associated to transmitter and receiver hardware imperfections are not included:

$$P_r = \frac{P_t G_t A_r}{(4\pi)^2 r_t^2 r_r^2}\sigma \qquad (W)\,. \tag{2.5}$$

However, the most common situation in active microwave remote sensing is that the transmitter and receiver are on the same location, as well as the use of the same satellite-borne antenna for transmitting and receiving of the microwave energy. Thus, for monostatic radars the parameters distance ($r_t = r_t = r$), gain ($G_t = G_r = G$) and effective apertures ($A_t = A_r = A$) are the same. In order to put the effective aperture (A) into terms of gain (G), the following relationship is introduced:

$$A = \frac{\lambda^2 G}{4\pi} \qquad (m^2)\,, \tag{2.6}$$

where λ is the wavelength of the radar system. Therefore, the *monostatic radar equation* can be defined as:

$$P_r = \frac{P_t G^2 \lambda^2}{(4\pi)^3 r^4}\sigma = \frac{P_t A^2}{4\pi\lambda^2 r^4}\sigma \qquad (W)\,. \tag{2.7}$$

where two forms are given, the first one related to the antenna gain and the second one of the antenna area.

The radar cross section σ is not defined in terms of any characteristics of a target type, thus, the radar equations (2.5) and (2.7) are general equations for both point and area targets, respectively. The radar cross section is a measure of reflective strength of a target in a given direction when it is hit by an incident electromagnetic wave (radar cross section = geometric cross section × reflectivity × directivity). It can also be represented as the ratio between the power that is reflected toward the receiver and the power intercepted to the object, or as

commonly written in electromagnetic analysis with $\mathbf{E}_s$ and $\mathbf{E}_i$, the far scattered and incident electric field intensities:

$$\sigma = 4\pi r^2 \frac{P_{\text{backscattered}}}{P_{\text{incident}}} = \lim_{r\to\infty} 4\pi r^2 \frac{|\mathbf{E}_s|^2}{|\mathbf{E}_i|^2} \qquad (m^2)\,. \tag{2.8}$$

Another interpretation of the radar cross section is, that if the object size spans several wavelengths, the radar cross section of the target is equal to the cross-sectional area of a perfectly conducting sphere that would produce the same magnitude of reflection as that observed from the target object.

The determination of the radar equation is based on the basic scattering model that individual point scatterers are fairly distributed on the illuminated target area, whereby none of these has a dominant scattering behaviour. This concept, for such distributed targets, allows to define a so-called *normalised radar cross section*, or also referred to *(back)scattering coefficient*:

$$\sigma^0 = \frac{\mathrm{d}\sigma}{\mathrm{d}A} \qquad \left(\frac{m^2}{m^2}\right), \tag{2.9}$$

as the differential scattering cross section $\mathrm{d}\sigma$ per differential unit area $\mathrm{d}A$. This new expression applied to the monostatic radar equation (2.6), assuming an extensive target, yields to:

$$P_r = \frac{\lambda^2}{(4\pi)^3} \int_A \frac{P_t G^2}{r^4} \sigma^0 \mathrm{d}A \qquad (W)\,. \tag{2.10}$$

This area-extensive representation of the radar equation is mostly used for remote sensing radars. But keep in mind the limitation of the underlying concept. As long as the signal is not dominated by one or a few targets, the concept might be appropriate. However, it needs to be clarified if this concept is applicable in any particular case.

A general formula allows to estimate σ^0 if the power received at the sensor (P_r) will be given:

$$\sigma^0 = P_r \cdot \frac{(4\pi)^3 r^4}{A P_t G^2 \lambda^2} \qquad \left(\frac{m^2}{m^2}\right). \tag{2.11}$$

In addition, most often σ^0 is converted into the logarithmically domain, due to the high dynamic range and for displaying purpose:

$$\sigma^0_{dB} = 10 \log \sigma^0 \qquad (dB)\,. \tag{2.12}$$

2.1.2 Resolution

The resolution of a radar is defined in two directions: parallel and perpendicular to the direction of movement. The term *azimuth resolution* is used in parallel flight direction, whereas *range resolution* in the direction perpendicular. Figure 2.3 shows the geometry of side-looking real aperture radar. The antenna is mounted on a moving platform pointing sideways and illuminating a small part of the continuous swath. The resolution of this *footprint* on the ground can be decomposed into range and azimuth resolution, which in general are dependent on the geometry and system parameters.

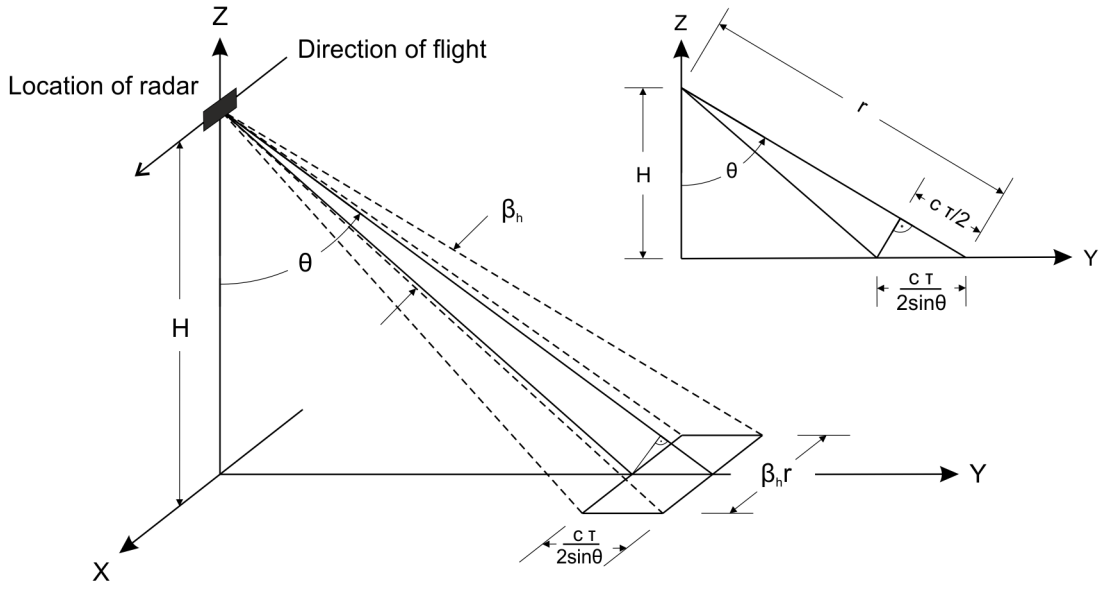

Figure 2.3: Geometry of a side-looking real aperture radar (after Ulaby et al. (1982)).

The determination of the range resolution is dependent upon the type of the radar system, either it is *pulse* or *frequency modulated* (FM). In the first case the pulse length is the crucial parameter, whereas in the second case the bandwidth is the important one. The relationship between the bandwidth B and pulse length τ is usually defined as:

$$B = \frac{1}{\tau} \qquad \left(\frac{1}{s}\right). \tag{2.13}$$

Thus, a shorter desired pulse requires a wider spectrum in order to be generated and detected. This would also require a high-voltage power supply, which is unfortunately a limitation on spaceborne instruments.

In order to derive the *ground range resolution*, which quantifies the ability to discriminate between features that actually lie on the Earth's surface, it is necessary to define first the *slant range resolution*, which is a system-limited parameter that is totally independent of the target under observation:

$$s_r = \frac{c\tau}{2} = \frac{c}{2B} \qquad (m)\,. \tag{2.14}$$

Using the connection from equation (2.13), the equation (2.14) above is given in two forms: The first case is related pulse length τ and the second case to bandwidth B. The parameter c denotes the velocity of propagation of the wave and the factor 2 result from the fact that the radar signal must travel to the target and back to the sensor. Equation (2.14) shows that short pulses or a large bandwidth provide a better range resolution. But as already mentioned, this would require a high-voltage power supply. A way around this challenge is a technique called *pulse compression*, where a long pulse has a bandwidth corresponding to a short pulse. This could either be achieved by phase coding or frequency modulation. Thus, the transmitter power can be reduced and still achieve the desired range resolution. The advantages of this technique generally outweigh the disadvantages, which are related to an addition transmitter and receiver complexity and struggling with time sidelobes. Therefore pulse compression is widely used.

The slant range resolution s_r is constant across the entire incidence angle range, but in order to get the ground range resolution g_r, the slant range resolution needs to be projected on the ground. This can either be formulated using the depression angle β or the incidence angle θ:

$$g_r = \frac{c\tau}{2\cos\beta} = \frac{c\tau}{2\sin\theta} \qquad (m)\,, \tag{2.15}$$

When the incidence angle becomes zero ($\theta = 0°$), in other words looking into nadir direction, the ground range resolution g_r becomes infinitely large. On the other hand, if the sensor is looking at the horizon ($\theta = 90°$), the range resolution is at minimum, which is equal to the slant range resolution ($g_r = s_r$). Thus, the ground range resolution is fairly unique in that it improves from the near to the far range.

The azimuth resolution is determined by the type of the radar system, as well as the operational parameters. In case of a real aperture radar system it is very simply defined by the beam width β_h and the distance in the slant range r:

$$a_r = \beta_h r \qquad (m)\,. \tag{2.16}$$

The beam width β_r represents the width of the area being illuminated. Thus, the best azimuth resolution with a real aperture radar is in the near range and decreases in a linear fashion with increasing distance from the sensor. Another expression of the beam width in terms of the wavelength λ and physical length of the radar antenna l yields to:

$$\beta_h = \frac{\lambda}{l} \qquad \left(\frac{m}{m}\right), \tag{2.17}$$

and therefore using equation (2.17) within (2.16) the azimuth resolution of a real aperture radar can also be formulated as:

$$a_r = r\frac{\lambda}{l} \qquad (m). \tag{2.18}$$

Now it is apparent that in addition to the distance r also two other parameters can be varied in order to increase the azimuth resolution. The equation (2.18) can be further expanded in order to understand other parameters influencing the azimuth resolution. Simple trigonometry can be used to describe the slant range (r) with the altitude (H) together with the incidence angle (θ) or depression angle (β):

$$r = \frac{H}{\sin\beta} = \frac{H}{\cos\theta} \qquad (m). \tag{2.19}$$

This can be used to substitute the slant range in equation (2.18), which yields to:

$$a_r = \left(\frac{H}{\sin\beta}\right)\frac{\lambda}{l} = \left(\frac{H}{\cos\theta}\right)\frac{\lambda}{l} \qquad (m). \tag{2.20}$$

The equation (2.20) shows that azimuth resolution in case of real aperture radar is actually dependent on different system parameters like altitude, wavelength or antenna length. It can be seen that with increasing incident angle (θ) or decreasing depression angle (β) and increasing altitude (H) the spatial resolution decreases. On the other hand a shorter wavelength would increase the azimuth resolution, which in turn changes also the sensitivity to surface roughness, as well as penetration depth. Another way of improving the spatial resolution can be achieved by a lower altitude, but this would also result in a reduction of the area covered or swath width for a given range of θ. Therefore, one might find a trade-off between those parameters in order to tune the radar for its applications.

The azimuth resolution in case of a synthetic aperture radar (SAR) system is completely different compared to a real aperture radar. A SAR system allows to synthesize a larger antenna by processing multiple acquisitions of a target passing by. The limitation of such a radar system is related to stability of the antenna and the duration of the time the target is in the radar beam. The equation for the maximum azimuth resolution in case of a point target can be simply given by:

$$a_s = \frac{l}{2} \qquad (m)\,. \tag{2.21}$$

This means the azimuth resolution is independent of range distance or instrument altitude. Thus, theoretically the spatial resolution of a SAR system carried by an aircraft platform will be the same for a spacecraft. But of course there is a limitation, which is related to the coherent nature of the SAR signal that results in *speckle* or *fading*.

2.1.3 Calibration

Calibration is the quantitative description of an instrument performance, which is important to understand the quality of the recorded data. In the majority of cases the raw output data is the electrical signal detected at the receiver, which needs to be related to the physical property of interest. Therefore, the determination of the relationship between the raw output data and the physical property needs to be investigated for any given instrument. It is important to identify how well this relationship is known, given that all systems contribute noise to the final detected signal (*Woodhouse*, 2006). Unfortunately, the noise signal is difficult to define theoretically before the instrument is operational, but at least it should be possible to experiment with some artificial signals in order to quantify the noise contribution right in the beginning. The assessment of the relationship and its noise-related uncertainty is referred to as *calibration*. If the calibration permits repeatable acquisitions, the system has a good relative calibration (*Ulaby et al.*, 1982). A good relative calibration allows fine distinctions between different target areas, as well as a precise change detection within the same target area. But bias errors which stay constant all the time are not detectable. Therefore an *absolute calibration* is important, which will ensure that the direct relationship is known quantitatively. In case of spaceborne scatterometery two different types of external references are used to calibrate the instrument in space: stable natural targets (distributed targets) and/or transponders (point targets).

2.2 ASCAT on board METOP-A

The European contribution within the framework of the Initial Joint Polar System (IJPS) is the EUMETSAT Polar System (EPS). The IJPS represents an agreement between the National Oceanic and Atmospheric Administration (NOAA) and the European Organisation for the Exploitation of Meteorological Satellites (EUMETSAT). It encompasses two polar-orbiting satellite systems, in order to provide and improve the operational meteorological and environmental forecasting monitoring services worldwide. The IJPS program contributes and supports the following systems and programs: the World Meteorological Organisation (WMO) Global Observing System, the Global Climate Observing System, the United Nations Environmental Programme (UNEP), the Intergovernmental Oceanographic Commission (IOC) and other related programmes. The EPS is set up to provide the morning (a.m.) orbit, whereas the American satellites continues to cover the afternoon (p.m.). As a result, the European and American satellites carry a set of identical sensors (AVHRR/3, AMSU-A, HIRS/4, MHS) (*Klaes et al.*, 2007; *NOAA*, 2011).

The space segment of the EPS programme is envisaged to contain three sun-synchronous Meteorological Operational Platforms (METOP-A, METOP-B and METOP-C) jointly developed by ESA and EUMETSAT. Each satellite has a nominal lifetime in orbit of about 5 years, with a planned 6 month overlap between consecutive satellites. The first METOP satellite was already successfully launched in 2006 from Baikonur Cosmodrome. The subsequent satellites will be launched in mid 2012 (METOP-B) and in 2016/2017 (METOP-C). This should allow an operational service proposed until 2020. The EPS ground segment consists a Mission Control Centre (MCC) located at the EUMETSAT headquarters in Darmstadt Germany, a Back-up Control Centre located at Instituto Nacional de Técnica Aeroespacial (INTA) in Torrejon de Ardoz, near Madrid, Spain and ground stations to communicate with the satellites in Spitsbergen, Svalbard (78° N). Satellite Application Facilities (SAF), which are spread over Europe, belong also the the ground network and are responsible to generate higher level products for specific meteorological applications (*EUMETSAT*, 2010).

A brief overview of the instruments on board METOP beside ASCAT is given below:

- an Advanced Very High Resolution Radiometer (AVHRR/3) to measure cloud cover, sea surface temperature, ice, snow and vegetation cover and characteristics,
- a High resolution Infrared Radiation Sounder HIRS/4 for humidity profiles, surface temperature, cloud parameters and total ozone,
- an Advanced Microwave Sounding Unit A1 and A2 (AMSU-A) for temperature sounding under clear and overcast conditions,

- a Microwave Humidity Sounder (MHS) to provide information on atmospheric water vapour,
- an Infrared Atmospheric Sounding Interferometer (ISASI) for temperature sounding, water vapour, and ozone monitoring,
- a Global Navigation Satellite System Receiver for Atmospheric Sounding (GRAS) for atmosphere sounding of temperature and humidity profiles,
- and a Global Ozone Monitoring Experiment (GOME) to measure radiation backscattered from the atmosphere and reflected from the earth surface in the UV and visible range.

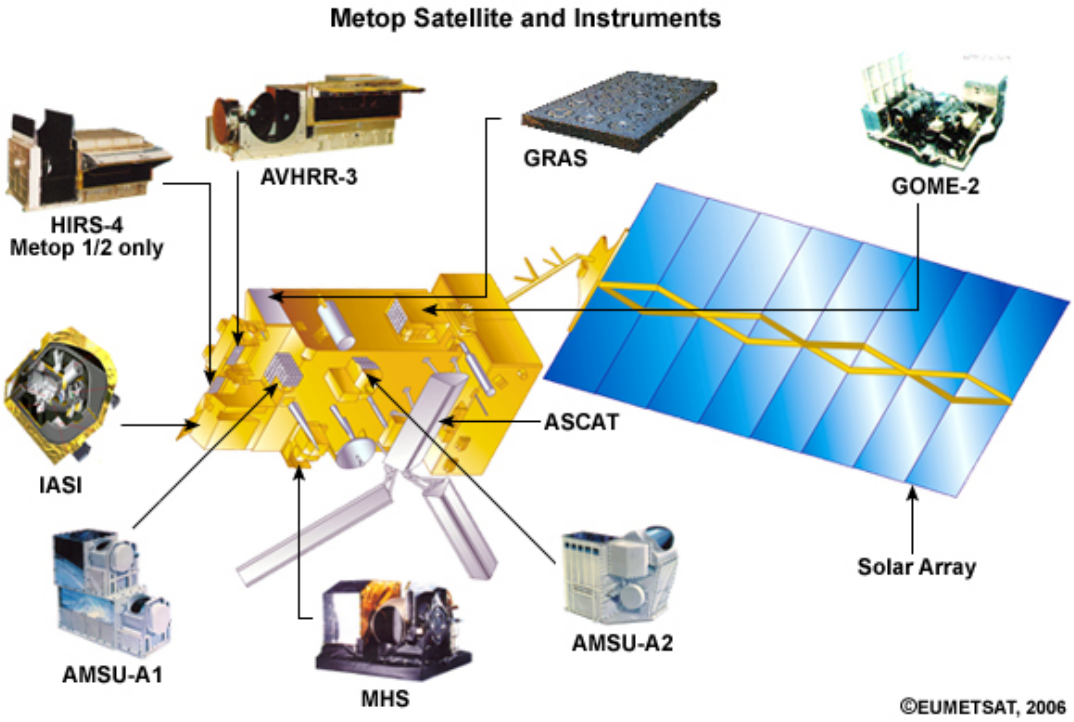

Figure 2.4: METOP-A payload (EUMETSAT, 2006).

2.2.1 Instrument description

ASCAT is a real aperture radar system operating in C-Band (VV polarisation) and will provide day- and night-time measurement capability, which is unaffected by cloud cover. The instrument design and performance specification is based on the experience of the AMI scatterometer flown on the ERS-1 and ERS-2 satellite. It can basically work in two different modes: Measurement or Calibration. The Measurement Mode is the only mode that generates science data for users. The instrument uses a pulse compression method called "chirp", at which long pulses with linear frequency modulation were generated at a carrier frequency of 5.255 GHz. After receiving and de-chirping of the ground echoes, a Fourier transform is applied in order to relate different frequencies in the signal to slant range distances. A preprocessing of the noise and echo measurements is done already on board to reduce the data rate to the ground stations, e.g. various averaging takes place reducing the raw data by a factor of approximately 25. Within each pulse repetition interval, after all pulse echoes have been decayed, the contribution of the thermal noise is monitored in order to perform a measurement noise subtraction during the ground processing. A side effect of on board processing is a degree of spatial correlation between different and within received echoes, but this is taken into account later on by the Level 1b processing. The radar pulse repetition frequency (PRF) is approximately 28.26 Hz, which yields to 4.71 Hz for the beam pulse repetition frequency in the sequence fore-, mid- and aft beam (*Gelsthorpe et al.*, 2000; *EUMETSAT*, 2009).

The Calibration Mode is used during external calibration campaigns (29 days every 13 months), when the platform passes over three different ground transponders located in central Turkey. The objective of such calibration campaigns is to verify that the backscatter measurements σ^0 from a target is correct for the whole incidence angle range. In other words, the absolute and relative calibration will be monitored and checked. A stable radar cross section and an accurately known position on the Earth's surface are the basic and important requirements for each transponder. After receiving a pulse from ASCAT, the active transponder send a delayed pulse back, which in turn can be recorded by ASCAT. A comparison between the localised transponder position and the expected data allows to estimate three depointing angles and gain correction values for each antenna. An east-west distribution with a displacement of approximately 150 km, will allow to obtain transponder measurements from most of the incidence angles for each antenna beam. This high sampling is necessary in order to reconstruct the characteristics of each antenna gain pattern for the whole incidence angle range and achieve an appropriate relative calibration. Such a calibration set up allows to establish a reference system in order to evaluate and monitor the instrument performance on regular basis (*Wilson et al.*, 2005, 2009).

Further independent investigations of the calibration quality include a comparison between σ^0 values measured over the ocean and a reference data set of σ^0 values derived from NWP model winds (*Stoffelen*, 1998) or natural targets such as ice sheets and tropical rain forest. In the latter case the backscatter behaviour is explained basically by volume scattering, which is typically isotropic, and therefore suitable for monitoring the absolute calibration (*Ulaby et al.*, 1982).

2.2.2 Geometry and coverage

METOP-A is flying in sun-synchronous 29 day repeat cycle orbit with an ascending node at 9:30 p.m. and a minimum orbit height of 822 km. This implies that METOP-A will make a little more than 14 orbits per day. An advanced measurement geometry of ASCAT allows twice the coverage, compared to its predecessors flying on ERS-1 and ERS-2 (see Figure 2.5). Thus, the daily global coverage increased from 41% to 82%. The spatial resolution was also improved from 50 km to 25 km, still reaching the same radiometric accuracy compared to the ERS-1/2 scatterometer.

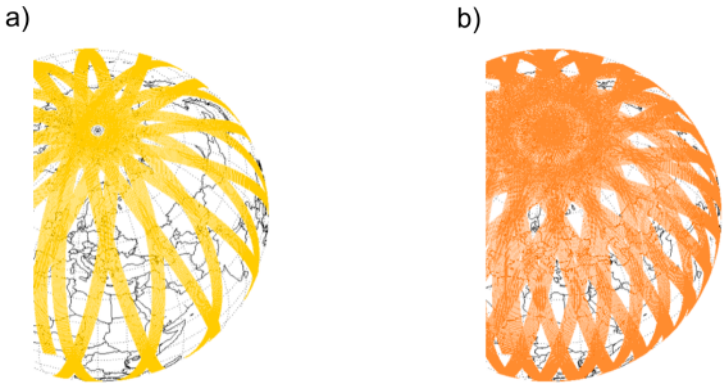

Figure 2.5: Daily coverage ERS-1/2 (a) and METOP-A (b) (from Bartalis (2009)).

The advanced global coverage capability is accomplished by two sets of three fan-beam antennas, compared to only one set at the ERS satellites. The fan-beams are arranged broadside and ±45° of broadside, thus, allowing to observe three azimuthal directions in each of its two 550 km swaths (see Figure 2.6). The swaths are separated from the satellite ground track by about 360 km for the minimum orbit height. Each point on the Earth's surface that falls within one of the two swaths, will be seen by all three antennas and a so-called σ^0 "triplet" can be observed. The incidence angles for those two antennas which are perpendicular to the flight direction intersect the surface between 25° and 53.3°, whereas the other four antennas have an incidence angle range from 33.7° to 64.5° (*Figa-Saldaña et al.*, 2002).

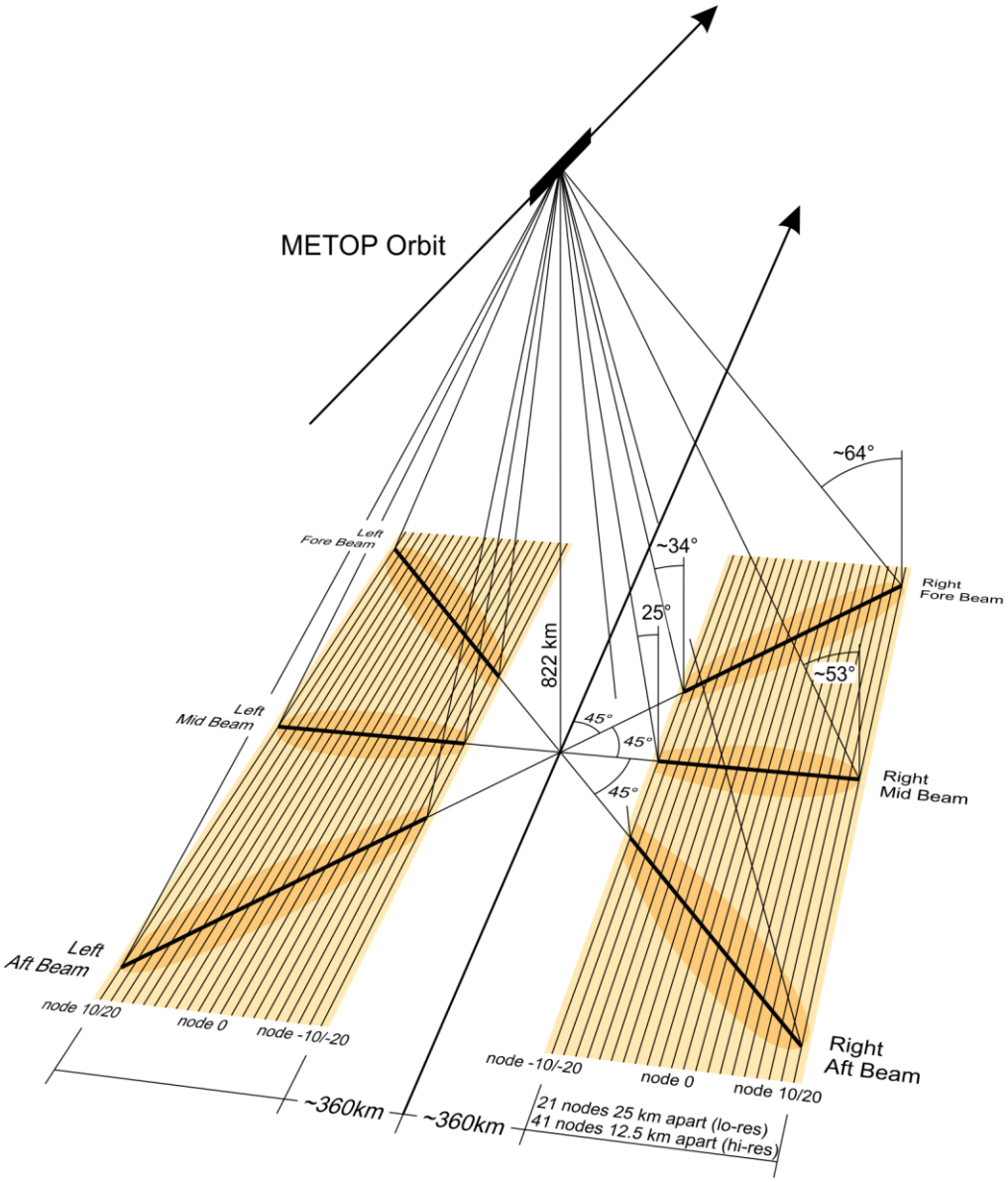

Figure 2.6: Measurement geometry of METOP-A ASCAT.

2.2.3 Product processing

Global data products are often classified into different levels according to their processing progress. In case of ASCAT the different product levels can be summarised as follows:

- **Level 0:** Unprocessed raw instrument data from the spacecraft. These are transmitted to the ground stations in binary form.
- **Level 1a:** Reformatted raw data together with already computed supplementary information (radiometric and geometric calibration) for the subsequent processing.
- **Level 1b:** Calibrated, georeferenced and quality controlled backscatter coefficients σ^0 in full resolution or spatially averaged. It includes also ancillary engineering and auxiliary data.
- **Level 2:** Georeferenced measurements converted to geophysical parameters, at the same spatial and temporal resolution as the Level 1b data.
- **Level 3:** Geophysical products derived from Level 2 data, which are either resampled or gridded points.

The raw data arriving at the ground processing facility are passed into the Level 1 ground processor. This data driven processing chain generates radiometrically calibrated Level 1b backscatter coefficients. It also includes an external calibration processing chain in order to support the localisation and normalisation process of the measurement power echoes. Before satellite launch, it is only possible to estimate parameters characterising the expected instrument performance, since some of them depend on in-flight conditions. But once the satellite is his orbit, these parameters can be assessed during a calibration campaign.

The first intermediate product generated just before the swath node generation and spatial averaging steps, is called Level 1b full resolution product. The main geophysical parameter in this product is the normalised backscatter coefficient σ^0. Along each antenna beam 256 σ^0 values are projected on the Earth's surface. The footprint size is about 10×20 km of various shapes and orientations, depending on the Doppler pattern over the surface. The radiometric accuracy and the inter-beam radiometric stability is expected to be lass then 0.5 dB peak-to-peak, whereas the georeferencing accuracy is about 4 km. In addition a number of quality flags are computed associated with every individual σ^0 sample along each antenna beam (*EUMETSAT*, 2009).

The other two products generated within the Level 1b processing are averaged σ^0 values at two different spatial grids. A two-dimensional Hamming window function centered at every grid node is used in both cases for spatial filtering. This weighting function is based on a cosine function, which will basically attenuate the contribution of values with increasing distance. The window width is deciding the magnitude of spatial resolution and which values contribute to the weighted result. This means, values beyond the window width are disregarded. The spatial resolution is then defined as the distance when the window function reaches 50% of its peak intensity. This spatial averaging is used in the along- and across-track direction, with the objective to generate a set of σ^0 "triplets" for each grid node of each swath at the desired radiometric resolution. The first product generated with this approach is called the nominal product and has a spatial resolution of 50 km for each grid point. The grid spacing is 25 km with 21 nodes at each swath per line. The higher resolution product has a spatial resolution ranging from 25 to 34 km. This variability is the result of a trade-off between spatial resolution and the desired radiometric accuracy, which lead to an alternating Hamming window width across the swath for the different beams. In this case the grid spacing is only 12.5 km, with 41 nodes at each swath per line.

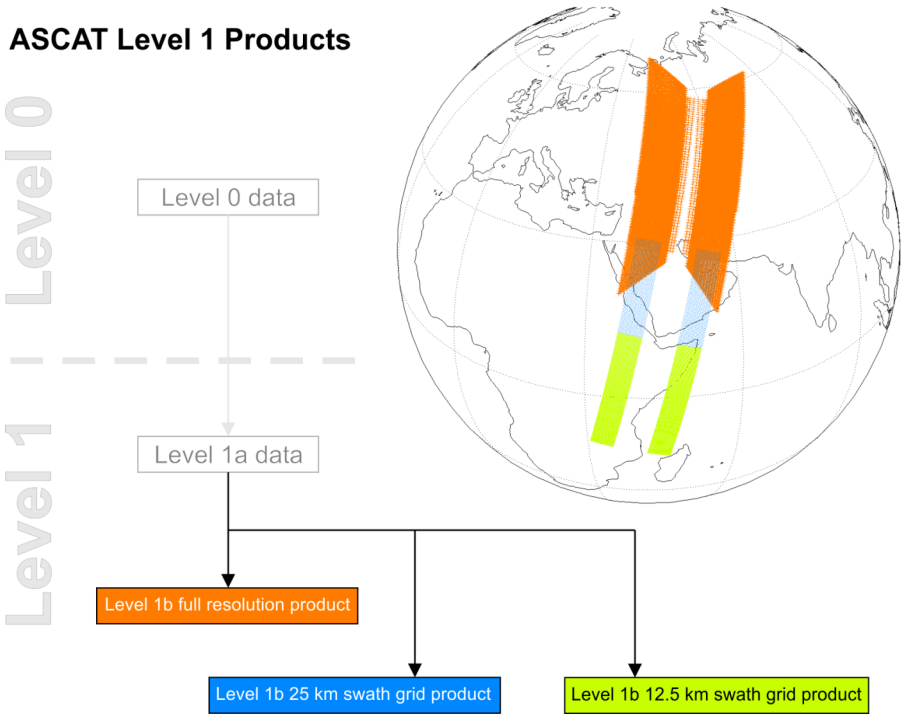

Figure 2.7: Overview of ASCAT Level 1 products.

The Level 2 ground processing consists of the derivation of winds near the ocean surface and soil moisture over land surfaces. The ASCAT ocean surface wind product is generated by the OSI SAF based on the radiometrically calibrated backscatter values from the 50 km Level 1b product. The near-surface ocean wind vectors are retrieved by using a Geophysical Model Function (GMF), which relates wind speed and direction to σ^0 values. The computation of wind vectors is an inversion problem, which in turn is difficult to solve due to ambiguities of the solutions yielded by the algorithms.

The ASCAT Level 2 soil moisture products are produced and distributed by EUMETSAT. The retrieval method for this product was developed by the Institute for Photogrammetry and Remote Sensing of the Vienna University of Technology. An insight about the algorithm will be given in the next chapter 3, as well as the implementation of the near real time processor WARP NRT used for the soil moisture retrieval by EUMETSAT. The current Level 2 soil moisture product is the so-called initial ASCAT soil moisture product, since an update of model parameters is still pending.

Chapter 3

Soil moisture retrieval at the Vienna University of Technology

The soil moisture product provided by the Vienna University of Technology is based on the TU-Wien soil moisture retrieval method, which was initially introduced by *Wagner* (1998) and recently improved by *Naeimi* (2009). The algorithm was originally developed for the Active Microwave Instrument (AMI) flown on the European satellites ERS-1 and ERS-2. A first global soil moisture product based on the TU-Wien soil moisture retrieval method with ERS-1/2 data was realised by *Scipal* (2002) and has shown meaningful results compared to in situ soil moisture observations (e.g. *Ceballos et al.* (2005)), modeled soil moisture (e.g. *Pellarin et al.* (2006); *Rüdiger et al.* (2009)) and precipitation data sets (e.g. *Wagner et al.* (2003); *Fontaine et al.* (2007)). In October 2006 a promising opportunity open up with the launch of the first of three METeorological Operational Platforms (METOP) carrying a new generation of scatterometer. The Advanced Scatterometer (ASCAT) on board METOP-A inherits and continues the role of the ERS scatterometers.

Notwithstanding that ASCAT has some improvements concerning the configuration and technical design, it is rather similar to the ERS scatterometers, whose cumulative experience was used to support the development of ASCAT (*Gelsthorpe et al.*, 2000; *Figa-Saldaña et al.*, 2002). Due to that fact the TU-Wien soil moisture retrieval method was expected to be almost directly applicable for ASCAT with only minor assimilation (*Bartalis et al.*, 2007). Since it is very critical to have a robust historic long-term reference database of scattering parameters available for the model, the initial ASCAT soil moisture product had to rely on the model parameters derived from ERS-1/2 data sets (01/1992-01/2001 and 08/2003-05/2007). But because of differences in absolute calibration and spatial resolution the combination of ASCAT backscatter measurements and ERS-1/2 historic long-term reference causes some problems in the initial ASCAT soil moisture product. The artefacts that thereby arise will be analyzed and investigated in Chapter 5.

3.1 TU-Wien Soil Moisture Retrieval Method

In general backscatter measurements from land surfaces depend to a mixture of surface and volume scattering effects. The radar penetration depth is dependent on the signal frequency, as well as on the composition of the target area. The impact of surface roughness, vegetation cover and terrain dielectric properties are important for the response of the land surface. The received energy at the sensor with respect to incidence angle has a characteristic behaviour for different targets. Thus, not only the backscatter intensity reveal an information about the situation on the ground, also the backscatter "slope" allows assessing surface type, vegetation cover and water content in the soil.

The concept of the soil moisture retrieval model developed at the Vienna University of Technology is a physical motivated empirical change detection method. The first realisation of the concept was based on ERS-1/2 data sets (*Wagner et al.*, 1999a,b) and later the same approach was successfully tested in combination with METOP-A scatterometer data (*Bartalis et al.*, 2007; *Naeimi et al.*, 2009). A high temporal resolution and multiple years of backscatter measurements form two basic requirements of the retrieval method. These demands are completely fulfilled in case of ERS-1/2, but the recent launch of METOP-A allowed to satisfy only the first requirement in the beginning. In addition, the multi-incidence angle viewing capability of both sensors are exploited in the model. The physical concept and mathematical formulation of the TU-Wien Soil Moisture Retrieval Model is described in *Wagner* (1998) and *Naeimi* (2009) in detail and shall be shortly summarised.

In the beginning the soil moisture retrieval was utilized only in specific regions (the Canadian Prairies, the African Sahel and areas with Mediterranean climate) covering major climate zones of the world. In the model soil moisture variations are extracted after observing and modeling the behaviour of the backscatter measurements σ^0. The characteristics of σ^0 reflects surface roughness, changes of vegetation and water content. An important fact is that each parameter acts on a different spatial and temporal scale. Considering these aspects, the TU-Wien model allows determining model parameters from long backscatter time series and building an essential knowledge on scattering effects for a certain position on the Earth's land surface. The underlying physical assumptions and empirically observed evidences can be summed up as follows:

- The incidence angle has a strong impact on the backscatter coefficient σ^0 of natural targets. This dependency is characteristic for roughness and vegetation, but soil moisture changes are not or only minimal affected by this circumstance.

- The incidence angle dependent backscatter $\sigma^0(\theta)$ is decreasing or increasing with vegetation grows, whether the contribution of the soil on the ground is higher than the contribution of the vegetation canopy or conversely. Hence, the $\sigma^0(\theta)$ time series are changing accordingly the vegetation phenology over the year.
- The vegetation phenology cycle influences σ^0 on a seasonal scale and local short-term variabilities are negligible due to the low resolution of the sensor.
- The relationship between soil moisture and σ^0, expressed in dB, is considered to be linear.
- There are certain incidence angles θ_{dry} and θ_{wet} at which σ^0 is rather stable in face of vegetation changes. These so called "crossover angles" are assumed to be 25° for the dry reference and 40° for the wet reference.
- The coarse resolution of the scatterometer admits the assumption that roughness and land cover are temporal invariant.

The upcoming subsections will address the major thoughts in the algorithm and their mathematical formulation. The details of those steps are described in *Wagner* (1998) and *Naeimi* (2009).

3.1.1 Normalisation

Since every backscattering coefficient σ^0 is acquired under a different azimuthal and incidence angle, those measurements are not directly comparable. Therefore it is necessary to apply a normalisation, so that all σ^0 refer to one common incidence angle and are corrected for azimuthal anisotropy.

Incidence angle dependency

In general the backscattered energy received by the sensor increases with decreasing incidence angle. The shape of such a curve is influenced by surface roughness, vegetation and water content in the soil (see Figure 3.1).

A second order polynomial is sufficient to describe the backscatter - incidence angle behaviour of such a curve. A Taylor polynom with an expansion point at 40° leads to:

$$\sigma^\circ(\theta, t) = \sigma^\circ(40, t) + \sigma'(40, t)(\theta - 40) + \frac{1}{2}\sigma''(40, t)(\theta - 40)^2 \,. \tag{3.1}$$

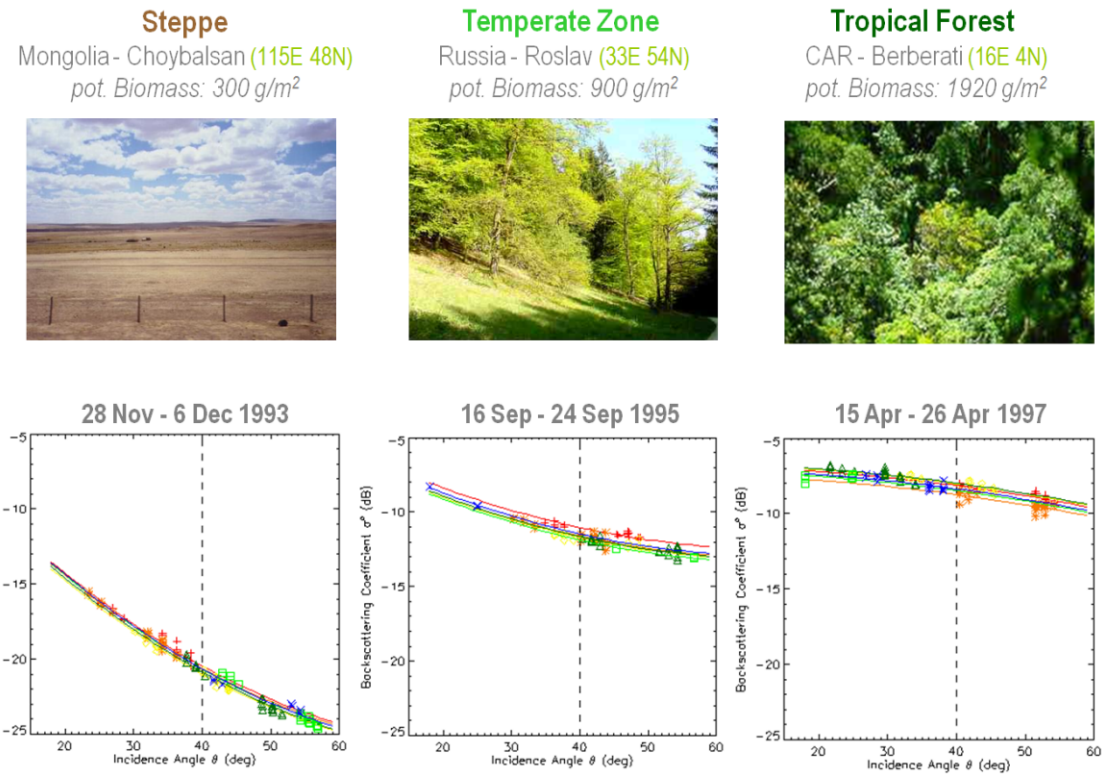

Figure 3.1: Backscatter behaviour for different biomes (from Scipal (2002)).

In equation (3.1) the σ' and σ'' are defined as the first and second derivatives of $\sigma(\theta)$. Furthermore, it is worth to note that in the equation above the slope σ' and curvature σ'' variables are changing over time. The Figure 3.2 shows a simple model of such variations if soil moisture increases or vegetation starts to grow. It illustrates that the gradient of the curve remains unchanged in case of soil moisture variations, whereby vegetation growth has a significant impact on the shape parameters: slope and curvature. However, the real magnitude of vegetation influence on the backscatter signal depends on the amount, size, orientation and tightness of the vegetation elements.

Due to the fact that soil moisture is considered to have no or negligible influence on slope and curvature (in other words slope and curvature are not sensitive to changes in dielectric properties), those two variables are expected to reflect the vegetation phenology circle and surface roughness for a certain point on the earth's surface. *Wagner* (1998) determined slope and curvature on a monthly basis and tried to fit a model using a function of the form:

$$\sigma'(40,t) = C' + D' + \Psi'(t)\,, \tag{3.2}$$

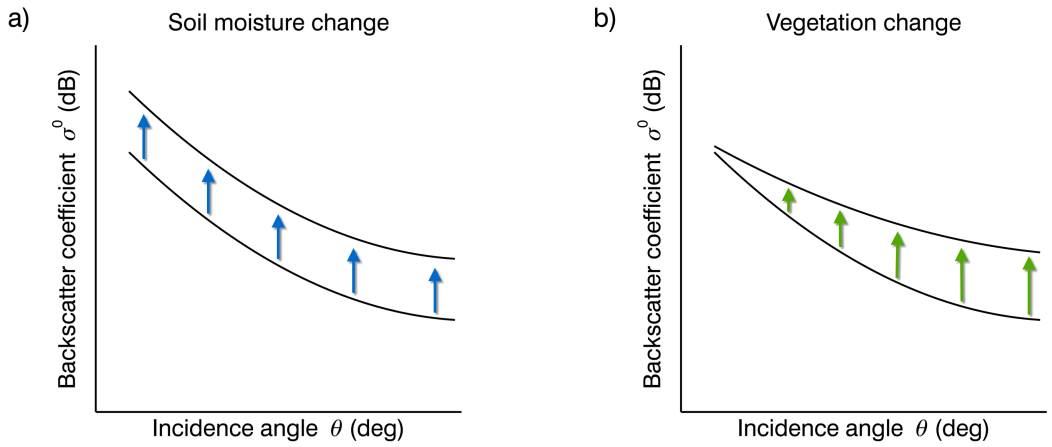

Figure 3.2: Incidence angle dependency of backscatter due to soil moisture (a) or vegetation (b) change.

where C' is a constant slope value, D' is the dynamic range of the slope and $\Psi'(t)$ is an empirical periodic function dependent on the region. But due to varying soil moisture conditions during every year and therefore different backscatter values, it is not accurately possible by simply fitting a polynomial to the historical backscatter measurements to specify the incidence angle dependency (*Naeimi*, 2009). Therefore the multi-incidence angle capability of the instrument is used to determine slope and curvature from local slope values extracted from simultaneous observations. The local slope can be derived individually by linear fitting (see Figure 3.3-a), using the σ^0 triplet:

$$\sigma'_L(\theta_L) = \frac{\sigma^0_m(\theta_m) - \sigma^0_{f,a}(\theta_{f,a})}{\theta_m - \theta_{f,a}}, \tag{3.3}$$

with

$$\theta_L = \frac{\theta_m + \theta_{f,a}}{2}. \tag{3.4}$$

The indices f, m and a represent the fore- mid- and aft beam of the instrument. It is worth mentioning that due to the geometry of the three antennas, the angle θ_m is always lower compared to the other two incidence angles $\theta_{a,f}$ for each σ^0 triplet. Furthermore, the local slope represents only an estimate of the real slope near the respective incidence angles, which is also affected by measurement noise. To determine the seasonal behaviour of slope $\sigma'(\theta,t)$ and curvature $\sigma''(\theta,t)$, the local slope values σ'_L will be calculated for each σ^0 triplet using neighbouring measurements in a given period τ centred on a selected day t.

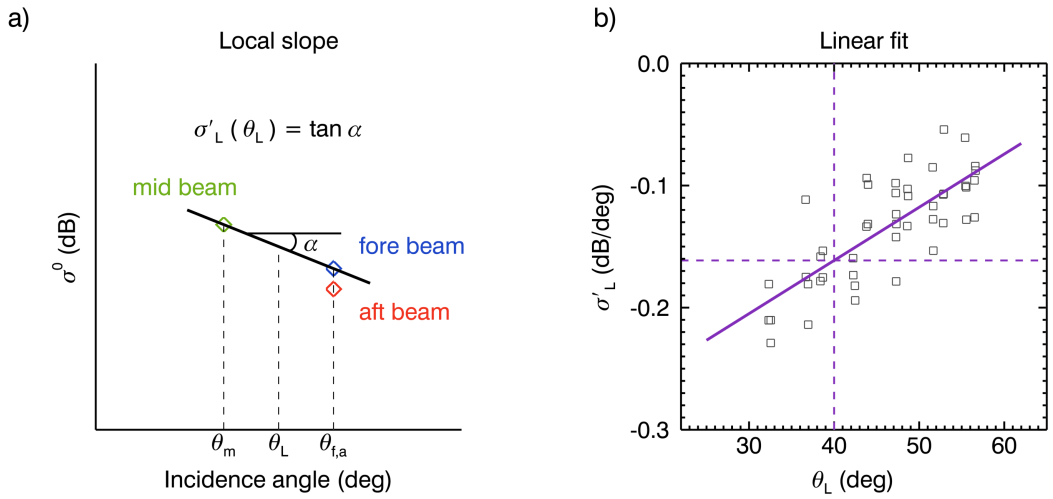

Figure 3.3: Calculation of local slope (a) and an example of linear fitting (b) through local slope values (GPI: 901858, Lat: 16.16°*, Lon:* 2.22°*).*

A linear fit through all local slope values σ'_L (see Figure 3.3-b) in this time window τ helps to identify the slope $\sigma'(40,t)$ and curvature $\sigma''(40,t)$ parameters at a 40° incidence angle, which will be used in equation (3.5) (rearranged notation of equation (3.1)) for the normalisation of the backscattering coefficients.

$$\sigma^0(40°,t) = \sigma^0(\theta,t) - \sigma'(40°,t)(\theta-40) - \frac{1}{2}\sigma''(40°,t)(\theta-40°)^2 \tag{3.5}$$

The selection of the time window length τ is critical. A too short period yields to noisy slope and curvature parameters, while a too long range could filter a remarkable part of the vegetation variation. Moreover, the window length is also dependent on the regional climate. Hence, to overcome the challenge for the right choice of the window length τ, a modified *Monte Carlo simulation* (*Niederreiter*, 1992) will be used with a series of different τ values (ranging between 2 and 12 weeks) as input. The result is a tube of many curves showing the annual characteristics of slope and curvature, whereby the outer limits can be considered as relative noise of σ' and σ''.

Azimuthal anisotropy

Due to the slight impact of azimuthal anisotropy over many parts of the world, a correction was neglected in the first model by *Wagner* (1998). At that time it was considered only as noise, which can be estimated as the difference between the backscattering coefficient from the fore (σ^0_f) and aft (σ^0_a) beam at the same incidence angle (see equation (3.6)). If a lot of

such pairs are available, the measurement noise can be removed and the mean value of δ shows the magnitude of azimuthal effects.

$$\delta = \sigma_f^0 - \sigma_a^0 \tag{3.6}$$

However, paying no attention on these effects will lead to artificial modulation of the signal in areas with a particular orientation of backscatter targets (e.g. mountainous regions, cities, desert areas). Therefore in the improved model presented by *Naeimi* (2009) an azimuthal correction is used based on a method described in *Bartalis et al.* (2006a).

3.1.2 Vegetation correction

The impact of soil moisture and vegetation changes on the behaviour of σ^0 is illustrated in Figure 3.2. As already mentioned, it is assumed that soil moisture variation do not or rather minimally affect the incidence angle dependency. In case of vegetation growth the slope and curvature changes significantly, which appears due to the fact that at mid to far incidence angles the fully-grown vegetation reflects more energy. But at near incidence angles the behaviour is exactly inverted. There, the received signal intensity decreases due to the attenuation of volume scattering from the vegetation canopy. This characteristic behaviour is visualised in Figure 3.4 in case of dry and wet soil.

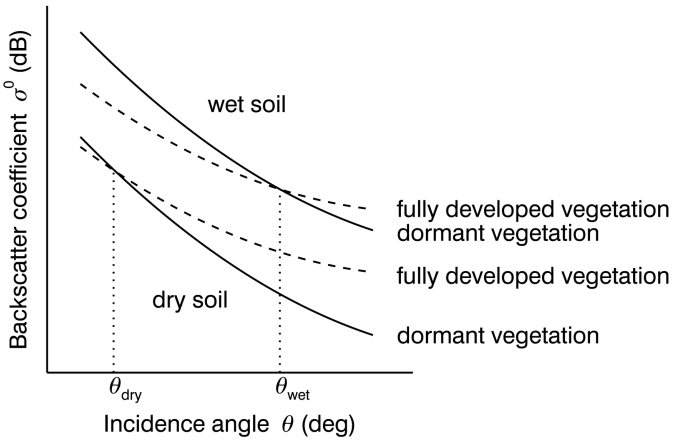

Figure 3.4: Crossover angle concept.

The outcome of Figure 3.4 is that there are certain incidence angles θ_{dry} and θ_{wet} at which σ^0 is rather stable in case of vegetation changes. These so called "crossover angles" are assumed to be 25° for the dry soil and 40° for the wet soil. This concept allows to compensate for vegetations effects, if the crossover angles are chosen correctly.

3.1.3 Surface soil moisture retrieval

The result of the TU-Wien soil moisture retrieval method is relative surface soil moisture, which is scaled between the historically lowest (σ^0_{dry}) and highest (σ^0_{wet}) values, which were acquired in the period covered by the available backscatter time series. For the determination of those values without any influence of vegetation it is important to convert the measurements to the respective crossover angle using

$$\sigma^0(\theta_{\text{dry}}, t) = \sigma^0(40°, t) + \sigma'(40°, t)(\theta_{\text{dry}} - 40°) + \frac{1}{2}\sigma''(40°, t)(\theta_{\text{dry}} - 40°)^2 , \tag{3.7}$$

for the dry reference and for the wet reference it is not necessary, since the normalisation angle and wet reference angle are equal. In order to ensure robust estimates for the dry and wet reference, an accurately removal of outliers is important. Therefore outliers are eliminated which are 3 interquartile ranges (IQR) below the first and above the third quartile. This action happens twice to provide a robust outliers removal. For the determination of the dry and wet reference the formally model used a fixed number of measurements, whereas the improved algorithm determines a dynamic number of measurements with respect to the noise level. Thus, a 95% confidence interval of the $\sigma^0(40)$ distribution is used to determine the number of measurements for the lower (N_{lower}) and upper limit (N_{upper}). The confidence interval for $\sigma^0(\theta_{\text{dry}})$ and $\sigma^0(\theta_{\text{wet}})$ can be calculated using the noise of $\sigma^0(40°)$ multiplied with 1.96, which represents the 97.5 percentile of the standard normal distribution:

$$\text{confidence intervall} = \pm 1.96 \times \text{noise of } \sigma^0(40°) . \tag{3.8}$$

Once the number of extreme measurements for the lower and upper limit are known, the dry and wet reference are calculated as the mean value:

$$\sigma^0_{\text{dry}}(\theta_{\text{dry}}) = \frac{1}{N_{\text{lower}}} \sum_{i=1}^{N_{\text{lower}}} \sigma^0_i(\theta_{\text{dry}}) \tag{3.9}$$

$$\sigma^0_{\text{wet}}(\theta_{\text{wet}}) = \frac{1}{N_{\text{upper}}} \sum_{i=1}^{N_{\text{upper}}} \sigma^0_i(\theta_{\text{wet}}) . \tag{3.10}$$

And only in case of dry reference $\sigma^0_{\text{dry}}(\theta_{\text{dry}})$ a transformation back to the normalisation angle is necessary using a rearranged notation of equation (3.7):

$$\sigma^0_{\text{dry}}(40°, t) = \sigma^0_{\text{dry}}(\theta_{\text{dry}}) - \sigma'(40°, t)(\theta_{\text{dry}} - 40°) - \frac{1}{2}\sigma''(40°, t)(\theta_{\text{dry}} - 40°)^2 . \tag{3.11}$$

Figure 3.5 illustrates the result of all previous steps for a location near Salamanca, Spain. A $\sigma^0(40°)$ time series together with the identified dry $\sigma^0_{\text{dry}}(40°, t)$ and wet $\sigma^0_{\text{wet}}(40°, t)$ reference. The bar chart in the bottom represent precipitation data from a nearby meteorological station. The response of the backscatter coefficient to rain events is apparently visible and also the vegetation phenology cycle captured by the dry reference.

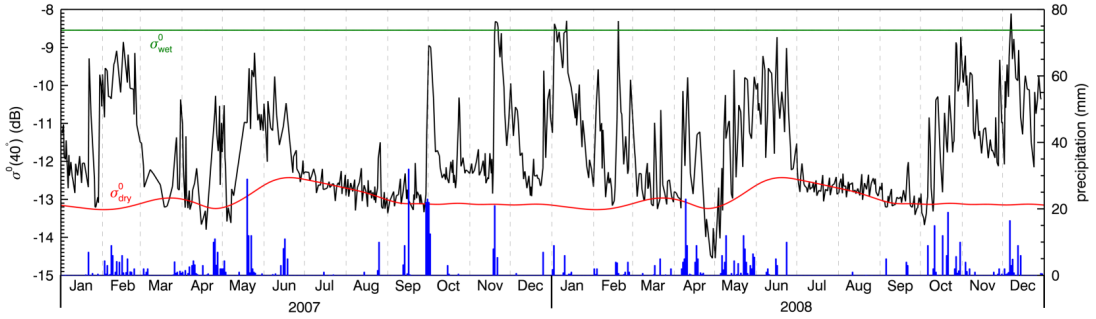

Figure 3.5: An example of $\sigma^0(40°)$ time series at a location near Salamanca, Spain (GPI: 2137584 - 41.08° *N,* 5.21° *W) for 2007-2008. The red and the green curves show σ^0_{dry} and σ^0_{wet}. The blue bar chart below represent precipitation data from a nearby meteorological station (WMO station:* 08202 - 40.95° *N,* 5.50° *W).*

A global map of $\sigma^0_{\text{wet}}(40°)$ and the lowest yearly $\sigma^0_{\text{dry}}(40°)$ (see (Figure 3.6)) give information about the captured dry and wet periods during the acquisition time span. The difference of those values describe the sensitivity related to soil moisture changes. A higher sensitivity enhance the quality of soil moisture retrieval.

But if a region is never captured in a truly saturated condition, which could be simply due to the fact that there were none, or they didn't occur during a satellite overpass, the sensitivity is abnormally low. Such a situation will lead to noisy looking time series, indicating escalated soil moisture conditions only due to a low sensitivity. In order to achieve an appropriate sensitivity in such regions it is necessary to make use of a so-called "wet correction". Since for the identification of such regions scatterometer measurements are not enough, an external climate dataset (*Kottek et al.*, 2006) will be used. The utilisation of the wet correction is done in 2 steps: first the lowest level of the wet reference is set to −10 dB, globally. Subsequently, in regions with rarely saturated soil moisture conditions (predominantly dry and hot climate zones) $\sigma^0_{\text{wet}}(40°)$ values are raised until the sensitivity reaches at least 5 dB (see Figure 3.7).

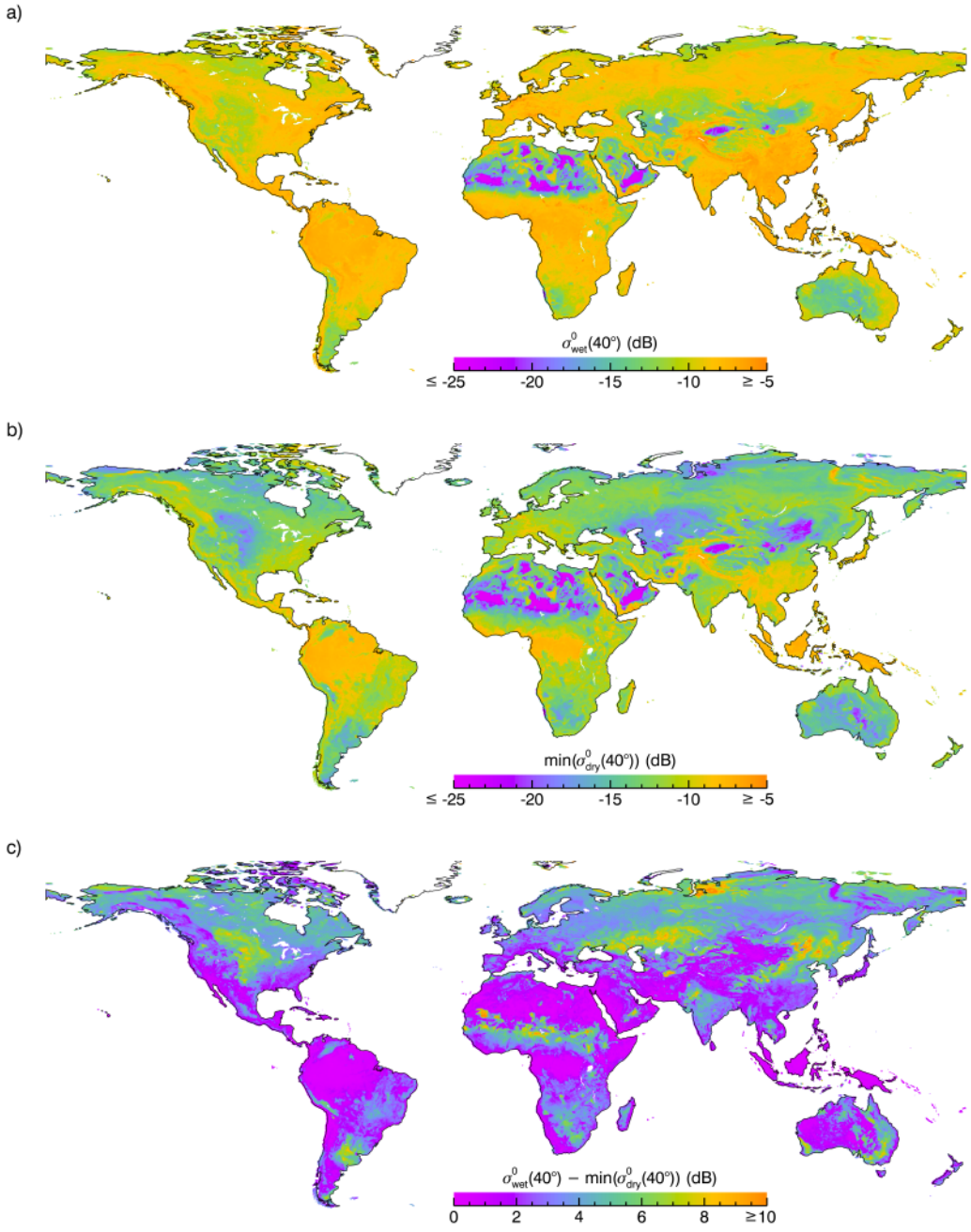

Figure 3.6: Wet backscatter reference (a), lowest dry backscatter reference (b) and sensitivity (c) derived from ASCAT (2007-2008).

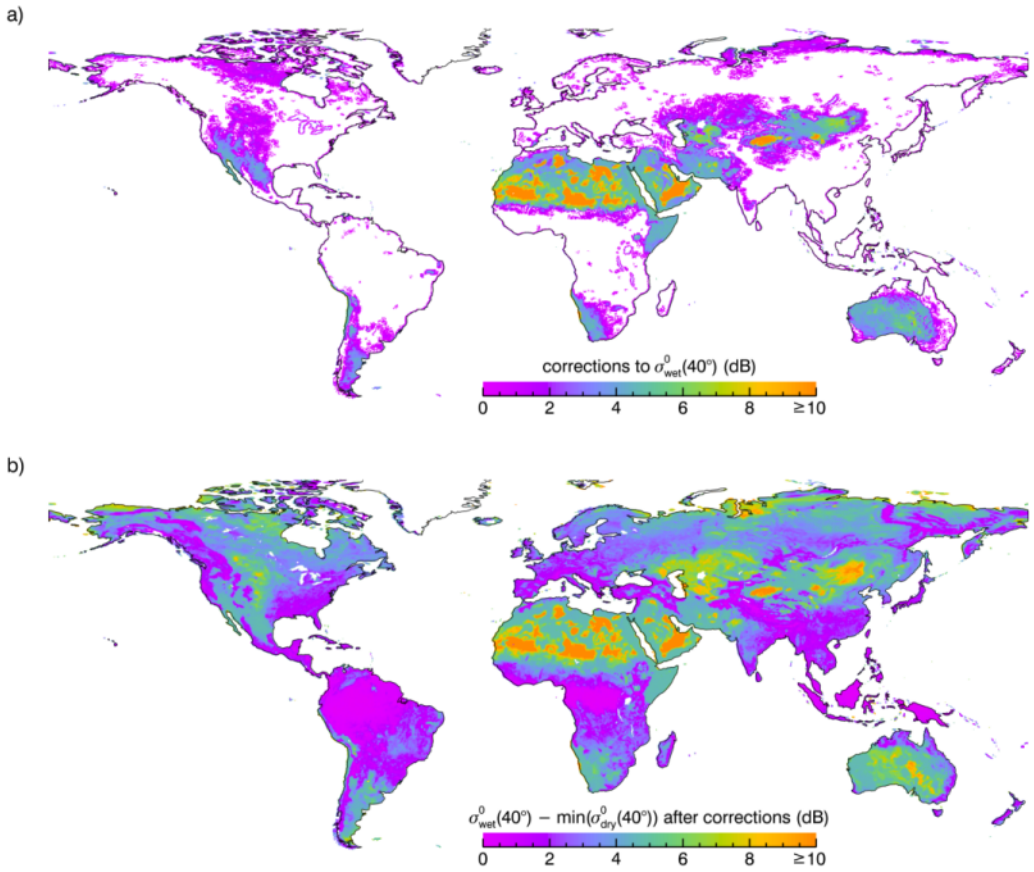

Figure 3.7: Wet correction (a) and sensitivity after correction (b).

Since it is assumed that soil moisture variations have a linear relationship to backscatter in the decibel domain, the last step is rather straightforward. The scaling of $\sigma^0(40°, t)$ values between $\sigma^0_{\text{dry}}(40°, t)$ and $\sigma^0_{\text{wet}}(40°, t)$ leads to relative surface soil moisture:

$$m_s(t) = \frac{\sigma^0(40°, t) - \sigma^0_{\text{dry}}(40°, t)}{\sigma^0_{\text{wet}}(40°, t) - \sigma^0_{\text{dry}}(40°, t)} \cdot 100 \qquad (\%)\,. \tag{3.12}$$

Due to the assessment of the lowest and highest reference, it is possible that relative surface soil moisture values can be below 0 or above 100 %. Such values are automatically flagged and set to their limits (0 and 100 %, respectively). In addition to the relative surface soil moisture m_s, the improved model also delivers a quantitative description of the noise level. For that purpose all uncertainty sources are analysed, collected and combined in an error propagation through the whole model.

3.2 WAter and Retrieval Package (WARP)

The technical realisation of the TU-Wien soil moisture retrieval method is the so called WAter and Retrieval Package (WARP). It has evolved over several versions from a command-line software tool for processing of small scatterometer data sets only, to a global processing system adapted to the current computer environment. A brief history of all versions is summarised in the upcoming enumeration:

- **Version 1** was ready in 1995 and included the routines for normalisation of the backscatter measurements and error models. The programming language at that time was the *Interactive Data Language* (IDL).
- **Version 2** has been completed during a fellowship at ESA and was written with the programming language *PV-Wave*. It included an advanced data base design and allowed the utilisation of the algorithm in different regions.
- **Version 3** was developed within the framework of an European Ph.D. fellowship programme at the Joint Research Center of the European Commission (JRC) in Ispra. Also this version was written in PV-Wave and has had included all important processing steps of the algorithm. Again, it was only applicable in small regions due to the underlying data base design.
- **Version 4** started from scratch with a new data base design and new data formats for global processing. Instead of PV-Wave it was decided to go back to IDL. It was the first version with a graphical user interface (GUI). The "Global Soil Moisture Archive 1992-2000 from ERS Scatterometer Data" was produced with this version of WARP (*Scipal*, 2002).
- **Version 5** is the latest update and still in use. The development of this version started again from scratch due to a lack of flexibility for algorithm updates in the previous version. An established fundamental library of IDL routines and positive experience induced the developers to stick to IDL for this version. The major updates includes a new discrete global grid (DGG), improvements in the model parameter computation and an error propagation, as well as the possibility to migrate the soil moisture retrieval from ERS-1/2 to METOP-A scatterometer data (*Naeimi*, 2009).

All those listed versions above are working offline, which means that the produced data sets were updated only on a half-yearly or yearly basis. This large intervals arise from the rare and expensive reprocessing actions. It is important to mention that all the processing is done

in the time domain. There are no explicit correlation calculations to neighbourhood pixels in the processing. As soon as the scatterometer measurements arrive in image format, the data is reorganised to a time series format in the first processing step. Only because of display and representation the data is transformed back to the spatial domain.

Apart from this offline generation of surface soil moisture at TU-Wien, an implementation plan for a near-real time (NRT) processor with the European Organisation for the Exploitation of Meteorological Satellites (EUMETSAT) was developed in 2005 (*Wagner*, 2005). The idea was to use and adapt the algorithm of WARP to develop a stand-alone software tool, which is able to retrieve soil moisture directly from the orbit data in near real time. As a result, WARP NRT is a rather small, batch-mode software system. On the other hand, WARP is much more complex and extensive. But to achieve all specifications, WARP NRT needs to rely on model parameters and look-up tables provided by the offline processor WARP. Therefore, in a strict sense, both WARP and WARP NRT form the Level 2 NRT soil moisture processor, although only WARP NRT needs to be considered in the operational environment.

	WARP	**WARP NRT**
Purpose	Processing of data archive	Operational processing
Programming language	IDL	C++
Processing strategy	Algorithms are applied to long-term time series on a discrete global grid (DGG)	Algorithms are applied to scatterometer data in orbit geometry
Inputs	ERS-1/2 and METOP-A scatterometer data	Near real time scatterometer data (METOP-A) and predefined model parameters (currently ERS-1/2)
Outputs	A long-term surface soil moisture time series and model parameters	Surface soil moisture in orbit geometry
Product update	Infrequently (half-yearly or yearly basis)	Near real time (approximately 135 minutes after acquisition)

Table 3.1: Comparison between WARP and WARP NRT (Wagner, 2005).

3.2.1 WARP 5.2

WARP 5.2 is the latest software version for the retrieval of surface soil moisture from scatterometer data realised with the programming language IDL. The system design consists an iterative approach for a stepwise derivation of model parameters and their combination for the final surface soil moisture retrieval. This elaborated concept allows to simplify algorithm updates in the future. Figure 3.8 shows a flowchart of the current WARP 5.2 processing chain.

The reviewed concept of the TU-Wien soil moisture retrieval model in the last section (3.1) is divided into several processing steps within WARP and can be shortly summarised as follows:

1. **Data resampling**
   The scatterometer data in orbit geometry is transformed into a time series format on a predefined discrete global grid (DGG). The DGG is generated by an adapted partitioning of the globe with an approximatively 12.5 km grid spacing (*Bartalis et al.*, 2006b). A hamming window function is used to resample the orbit data to the grid points. Until this point, all successive processing steps are applied to each time series separately.

2. **Azimuthal normalisation**
   Due to the reason that in some regions azimuthal anisotropy has a significant influence on σ^0, it is necessary to overcome this issue. Therefore a second order polynomial models the σ^0 variations with respect to the incidence angle for each azimuth combination. The difference between these polynomials and the polynomial derived for the whole data set is used as a correction bias (*Bartalis et al.*, 2006a).

3. **Estimated standard deviation of σ^0**
   The estimated standard deviation (ESD) of σ^0 describes the noise, speckle and residual azimuthal effects, based on difference between fore- and aft beam σ^0 values:

$$\mathrm{ESD}(\sigma^0) = \frac{\mathrm{StDev}(\sigma^0_f - \sigma^0_a)}{\sqrt{2}} \,. \tag{3.13}$$

   This should represent an estimate of the real standard deviation of the backscatter signal and serves as a first input for the error propagation.

4. **Determining the yearly cycle of the derivatives σ' and σ'' at $40°$**
   The characteristic behaviour for slope σ' and curvature σ'', which will be needed for the normalisation in the next processing step, are determined using the local slope. A linear fit through local slope values within a certain time window (τ) centered over a day in

question is used to get the σ' and σ'' values at 40°. The determination of the yearly circle of those values is realised by a method similar to a Monte Carlo simulation, where the final $\sigma'(40°, t)$ and $\sigma''(40°, t)$ values for each of the 366 days of the year are computed as the arithmetical mean of many annual curves, each calculated with a time window range between 2 and 12 weeks. Thus, to have a trade-off between a sensitive but noisy curve and a less susceptible but robust one due to vegetation phenology. The result of this processing step are a set of 366 values for each grid point containing following variables: σ' and σ'' at 40° and noise of σ' and σ'' at 40°.

5. **Calculating σ^0 at 40° and its noise**
   The parameters slope and curvature serve as input to equation (3.5) to derive $\sigma^0(40°, t)$ time series. The noise values will be obtained by continuing the previous error propagation.

6. **Calculating the dry σ^0_{dry} and wet σ^0_{wet} backscatter references at 40°**
   In the beginning of this processing step the $\sigma^0(40°, t)$ time series will transformed to the respective crossover angle for the dry and wet reference to minimise the effect of vegetation influence on the backscatter measurements. After a robust outliers removal, the extreme high and low values are separated with respect to an explicit uncertainty range, defined as a 95% 2-sided confidence interval. The mean values of those separated extreme observations represent the dry $\sigma^0(\theta_{\text{dry}})$ and wet $\sigma^0(\theta_{\text{wet}})$ reference. In the end, these references needs to be transformed back to the normalisation angle, thus leading to an annual cycle for $\sigma^0_{\text{dry}}(40°, t)$ and $\sigma^0_{\text{wet}}(40°, t)$. In addition, the wet reference needs to be corrected in arid areas with low sensitivity, due to a lack of capturing saturated conditions. Therefore an external climatology data set (*Kottek et al.*, 2006) will be used to determine these locations. The result of this processing step are 366 values for the dry $\sigma^0_{\text{dry}}(40°, t)$ and wet $\sigma^0_{\text{wet}}(40°, t)$ reference at each grid point.

7. **Calculating the surface soil moisture and its long-term mean**
   Based on equation (3.12) relative surface soil moisture $m_s(t)$ can be calculated, as well as a long-term mean using a moving average window of 30 days width over data from all available years. m_s represent a relative measure of the water content in the surface layer ranging between 0 and 100%.

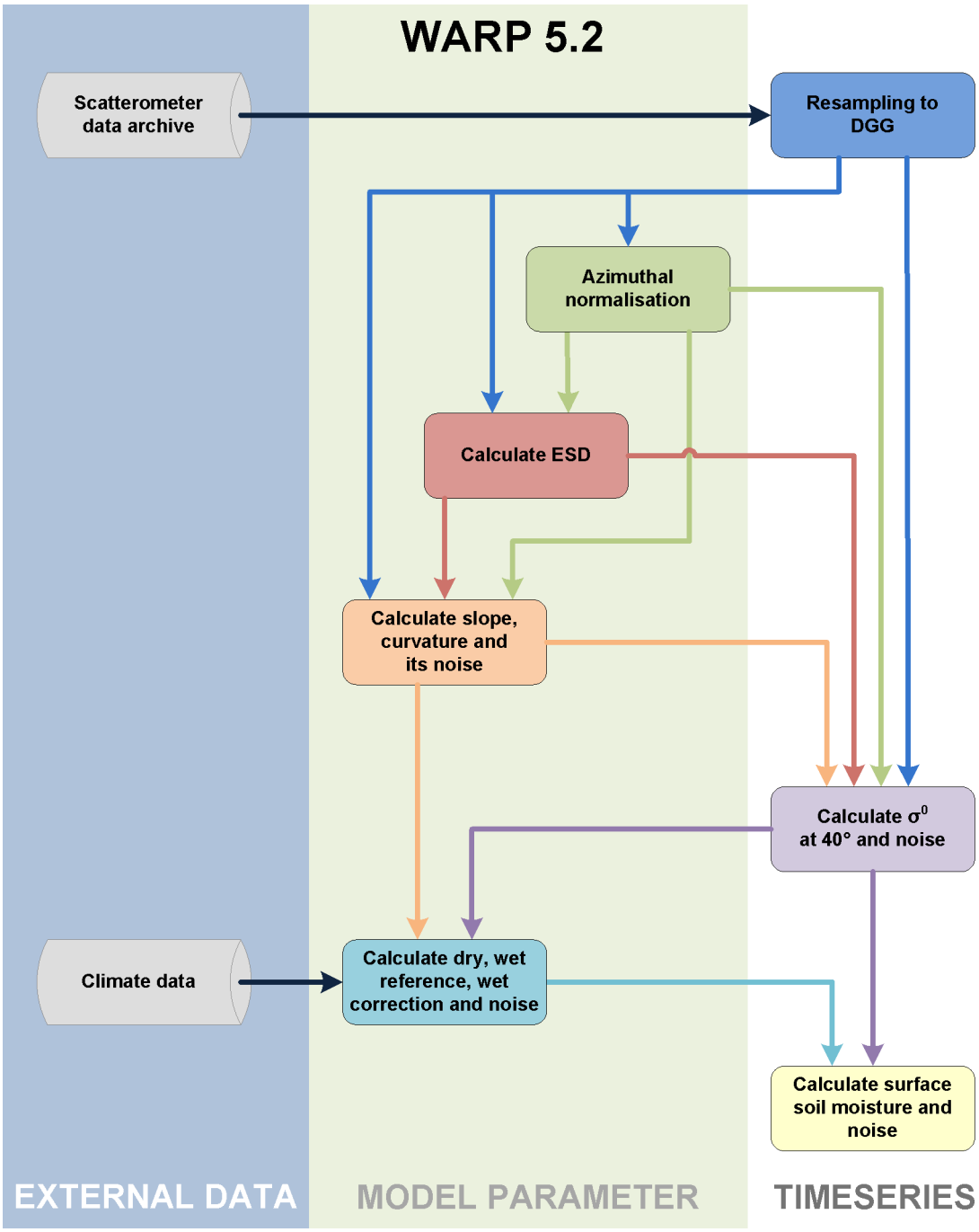

Figure 3.8: WARP 5.2 flowchart: the left column shows the external data, the column in the middle illustrates the processes generating model parameters and the right column processes producing data in time series format.

The major outcome of the WARP 5.2 processing chain are, beside model parameters (azimuthal correction polynomials, estimated standard deviation, dry and wet reference), relative surface soil moisture time series $m_s(t)$. The version WARP 5.0 was used to produce surface soil moisture from scatterometer data of ERS-1/2 at 50 km (01/1992-01/2001 and 08/2003-05/2007), whereas the updated version WARP 5.2 used METOP-A data (01/2007-09/2010) at 25 km spatial resolution. Although the idea in the beginning was to merge the data sets and use them together, they were processed separately. It was planned to cross-calibrate at least one year of overlapping data from ERS-2 at 25 km and METOP-A at 25 km. But since the inter-calibration bias between ERS-1/2 and ASCAT is not exactly known yet, this situation lead to two separated offline surface soil moisture products in different spatial resolutions and based on two different model parameter databases. Figure 3.9 illustrates the current situation of the offline reprocessing facility running at TU-Wien.

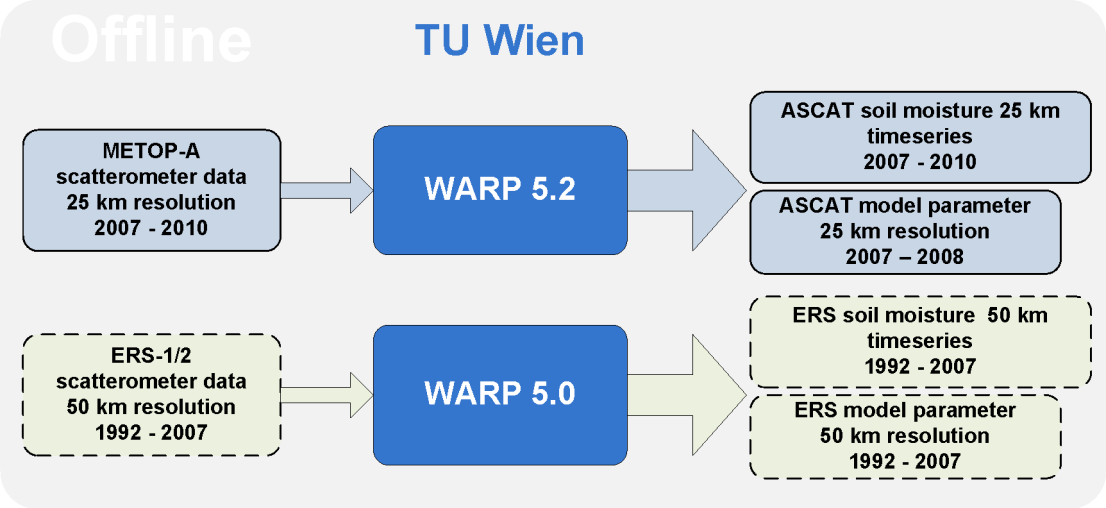

Figure 3.9: Offline soil moisture processing chain implemented at TU-Wien. The WARP processor once was executed together with ERS-1/2 and METOP-A scatterometer data separately. Thus, two separate soil moisture products in time series format, together with their corresponding model parameter, are currently available.

3.2.2 WARP NRT

The architecture of WARP NRT is in principle identical to WARP 5.2, but requires already computed model parameters and look-up tables. It would take too much time to compute such parameters on-the-fly. Since not enough ASCAT measurements were available in the beginning, the WARP NRT processor is dependent on the global long-term reference database derived from ERS-1/2 scatterometer data (01/1992-01/2001 and 08/2003-05/2007). A prototype of the processor was developed at TU-Wien and implemented at the EUMETSAT Ground Segment during 2008 with the programming language C++. The processing steps in the latest WARP NRT version 2.0 can be summarised as follows:

1. **Resampling**
   In the beginning time-independent model parameters needs to be loaded, which will be valuable for the later processing. After this, the ASCAT measurements in EPS format will be read and the time-dependent model parameter are restored. To make use of those model parameters in the processing, they need to be resampled from the DGG to the ASCAT swath grid. This will be accomplished with a hamming window function, always requiring at least three grid points with valid parameters.

2. **Calibration bias correction**
   This step applies a node- and beam-dependent bias correction for ASCAT backscatter measurements based on a table provided by the Royal Netherlands Meteorological Institute (KNMI).

3. **Normalisation**
   The prior loaded look-up tables help to normalise σ^0 with respect to their acquisition azimuth angle and incidence angle to derive $\sigma^0(40°)$ values.

4. **Soil moisture retrieval**
   A scaling of the ASCAT $\sigma^0(40°)$ values between the respective dry and wet reference admits the calculation of a relative surface soil moisture value. Also an estimated noise value is attached to the final soil moisture product.

5. **Flags assignment**
   In the end, among others, some climatological advisory flags related to probability of snow cover and frozen soil will be set. However, two important flags to mention are, the *processing flag*, which will be set whenever a soil moisture value could not be calculated, and the *correction flag*, which indicates an allowed adjustment to 0 or 100% relative surface soil moisture.

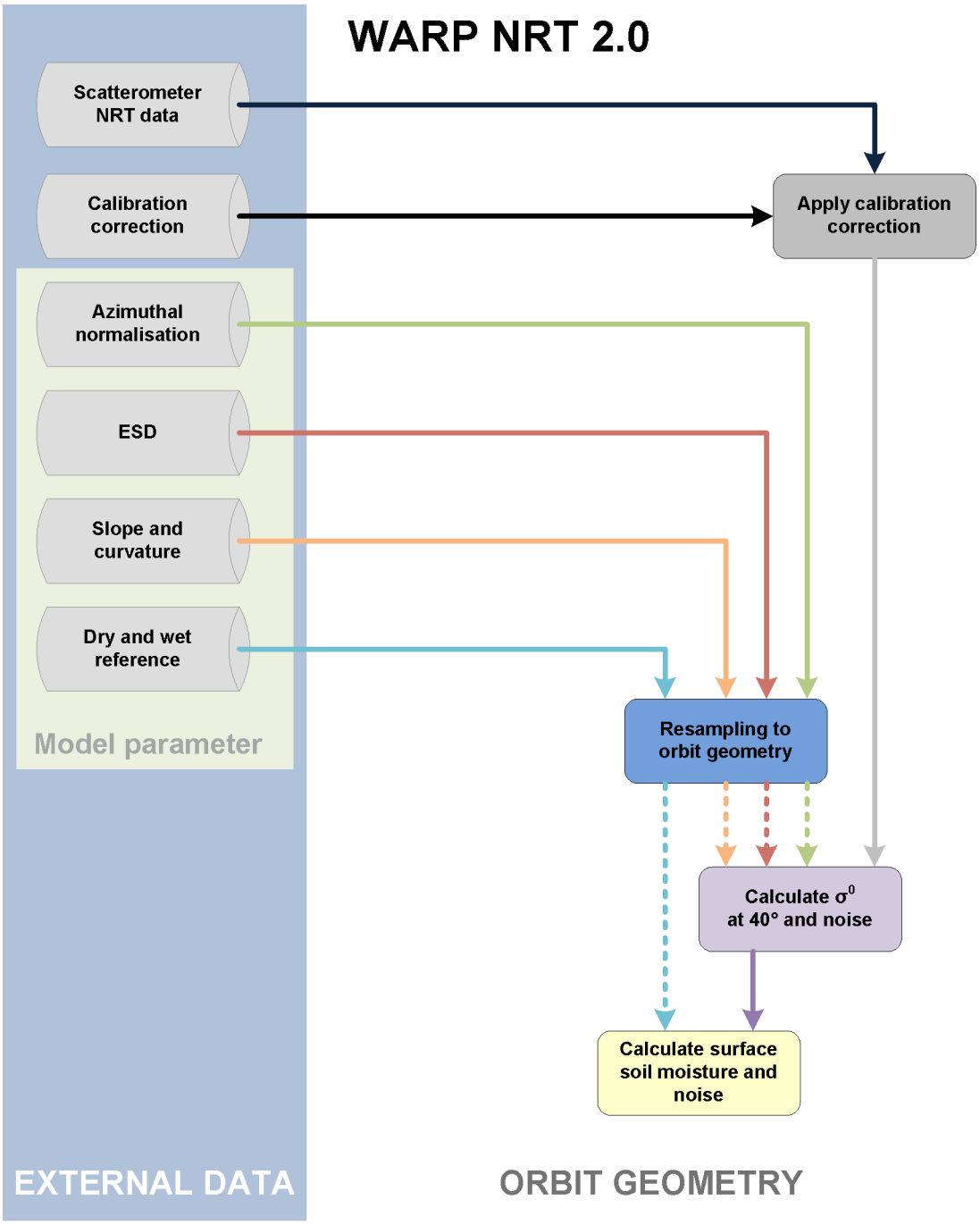

Figure 3.10: WARP NRT flowchart: the left column shows the external data on which WARP NRT rely. The product output format will be orbit geometry, as indicated in the right column.

The current result of the WARP NRT processing chain is the so-called initial ASCAT surface soil moisture product, which is available in two spatial resolutions, nominal (50 km) and research (25 km), respectively (see Figure 3.11). The term "initial" should indicate the combination of ASCAT backscatter measurements with the historic model parameters of ERS-1/2, which was considered only as an intermediate solution. But since the ERS-2 archive wasn't completely reprocessed by ESA so far, the merged model parameter database could not be established. Right now, there is a sufficient number of ASCAT measurements available in order to derive an independent model parameter database, which already happened for two years of ASCAT data (2007-2008) in the offline regime. But an update at EUMETSAT in the NRT environment isn't that trivial. Since meteorological users have already implemented the current soil moisture product in their assimilation systems, a change to a new model parameter database has farther reaching consequences. In the first place, the impact of new model parameters on the soil moisture product needs to be analysed and investigated, before users can slowly change to the new product. In addition, exhaustive reprocessing actions also prevent a fast switch to the updated product.

The actual conjunction of ASCAT Level 1B data with ERS-1/2 model parameters leads to artefacts in the initial ASCAT soil moisture product. A difference in the absolute calibration between ERS scatterometers and ASCAT, as well as a different spatial resolution in case of the 25 km research product, are expected to cause the strongest artefacts. While ASCAT was calibrated with three active ground transponders located in Turkey (*Wilson et al.*, 2005, 2009), ERS used a combination of short-term transponder campaigns and natural reference targets (*Lecomte and Wagner*, 1998). The resolution mismatch in the ASCAT research product arise due to the fact that the historic model parameters are only available in 50 km spatial resolution. Therefore, a simple model derived in the next chapter 4 should simulate the artefacts and their impact on the soil moisture product.

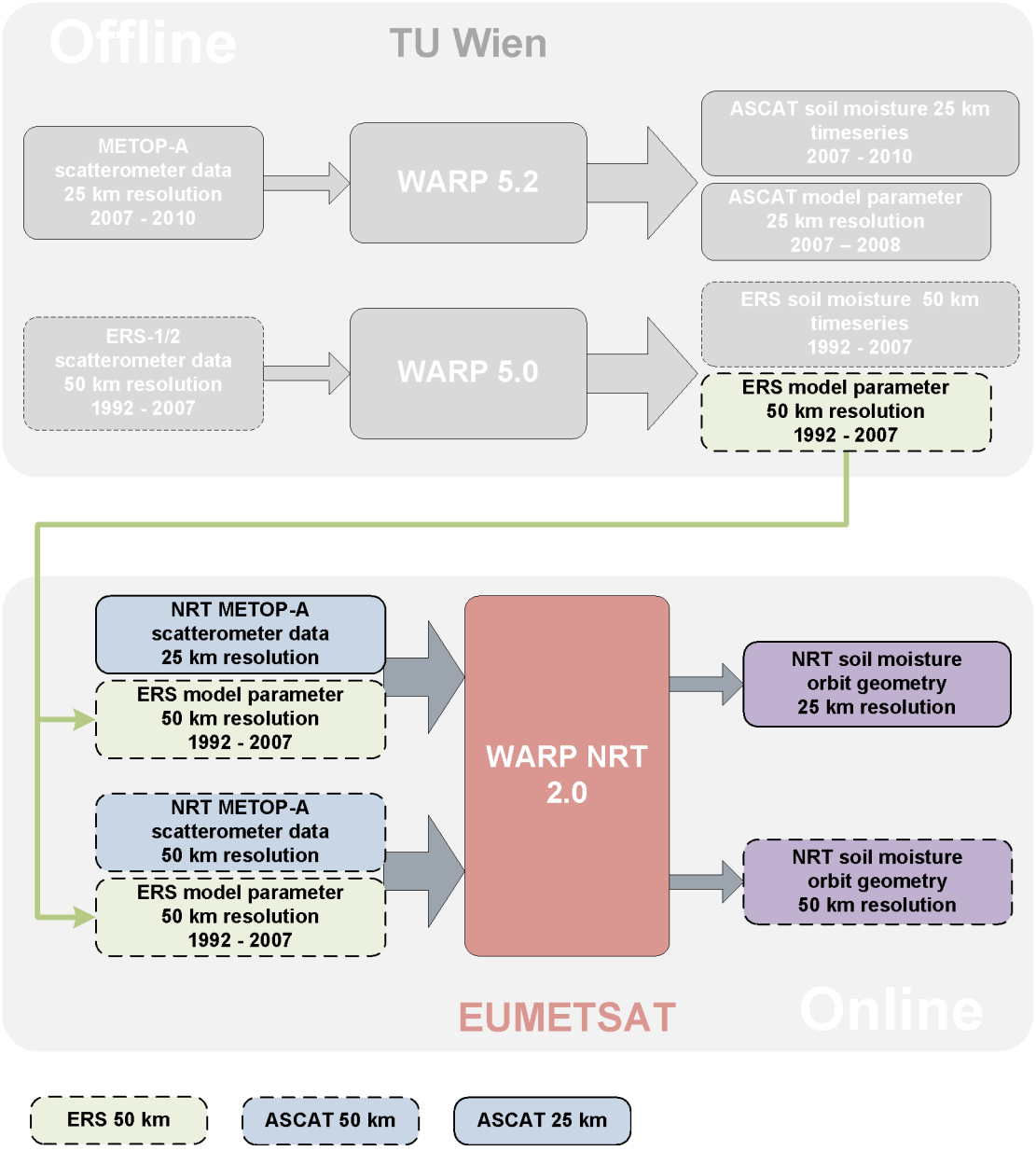

Figure 3.11: Online soil moisture processing chain implemented at EUMETSAT. The WARP NRT processor requires model parameters retrieved from the offline processing chain installed at TU-Wien. The two products generated by the NRT processor are the so called initial ASCAT surface soil moisture products.

Chapter 4

Characterisation of calibration-related soil moisture artefacts

The initial ASCAT soil moisture product is generated by the WARP NRT processor implemented in the EUMETSAT ground segment. The product is operationally since December 2008 and available in two different spatial resolutions, nominal (50 km) and research (25 km), respectively. In order to perform a robust and quick near real time soil moisture retrieval, WARP NRT needs already existing model parameters and look-up tables. Instead of using model parameters based on ASCAT data, which was of course not possible in the beginning, the processor had to rely on historic model parameters derived from ERS-1/2. This considered intermediate solution with an acceptance of loss in quality is still the state of the art. Therefore, a model was developed to investigate and quantify the impact of this mixture, which will be described in the upcoming sections.

Differences in the *Level 1 calibration* (absolute calibration) of the instruments and in case of the research product, a mismatch of spatial resolution, are the expected major causes for the remaining artefacts in the initial ASCAT soil moisture product. The resolution mismatch can also be seen as wrong *Level 2 calibration*, since the ERS-1/2 model parameters, only available in 50 km resolution, will be used for normalisation and retrieval of surface soil moisture from ASCAT 25 km σ^0 measurements. Thus, both causes represent calibration-related conflicts, which lead to soil moisture artefacts in certain areas. To minimize at least the effect of the different Level 1 calibration, a look-up table with bias corrections will be used in the WARP NRT processor provided by the Royal Netherlands Meteorological Institute (KNMI). Anyhow, the presented model will not consider this bias corrections applied in the operational domain, in order to investigate the effect of the presence of an absolute calibration difference as well.

4.1 Modelling consequences of calibration-related conflicts

The following model should quantify the impact of the conjunction between ASCAT and ERS-1/2 data sets on the NRT soil moisture retrieval. A detection of the affected areas, as well as an identification of the dominant cause and their magnitude of the artefacts are the major goals of this model. The model is constituted and adjusted for the ASCAT 25 km research product due to the additional mismatch of spatial resolution. The supplementary bias correction, which should accommodate for the different Level 1 calibration was neglected in the model to demonstrate the full impact of all calibration-related conflicts.

The starting point of the upcoming model is the scaling equation (3.12), which will be used for the final retrieval of surface soil moisture in the TU-Wien model. This approach should allow to build a simple model which is able to reveal information about the calibration issue. A time-independent parameterisation of equation (3.12) can be written as:

$$m_s(x,y) = \frac{\sigma^0(x) - \sigma^0_{\text{dry}}(y)}{\sigma^0_{\text{wet}}(y) - \sigma^0_{\text{dry}}(y)} \cdot 100\,, \tag{4.1}$$

where x characterises the type of input measurement and y the model parameter. The considered optimal solution would be that the input measurements σ^0, as well as the model parameters σ^0_{dry} and σ^0_{wet} come from the same instrument and resolution to be sure that there exists no calibration-related differences. In the ideal case of METOP-A the equation above would read:

$$m_s(\text{M25},\text{M25}) = \frac{\sigma^0(\text{M25}) - \sigma^0_{\text{dry}}(\text{M25})}{\text{sens}(\text{M25})} \cdot 100\,, \tag{4.2}$$

for the research product. The first letter of the parameter M25 represent an abbreviation of the satellite METOP-A, whereby the subsequent numbers indicate the spatial resolution of 25 km. The subtraction between wet and dry reference is summarised for the sake of convenience in one term only, called sensitivity (sens $= \sigma^0_{\text{wet}} - \sigma^0_{\text{dry}}$). However, the current situation looks different in case of WARP NRT due to the lack of model parameters retrieved from METOP-A scatterometer data. In this case, the parameterised equation (4.1) needs to be written as:

$$m_s(\text{M25},\text{E50}) = \frac{\sigma^0(\text{M25}) - \sigma^0_{\text{dry}}(\text{E50})}{\text{sens}(\text{E50})} \cdot 100\,. \tag{4.3}$$

In equation (4.3) the parameter E50 denotes data from ERS at 50 km resolution. The surface soil moisture value $m_s(\mathrm{M25},\mathrm{E50})$ is afflicted by artificial modulated anomalies, due to calibration-related conflicts between the ERS scatterometers and ASCAT. The quantification of these artefacts is possible by subtracting the current situation (equation (4.3)) and the optimal solution (equation (4.2)):

$$\Delta m_s = m_s(\mathrm{M25},\mathrm{E50}) - m_s(\mathrm{M25},\mathrm{M25})\,. \tag{4.4}$$

Indeed, the deviation Δm_s gives information about the differences on the soil moisture values immediately, but to simulate those effects for different soil moisture conditions directly, the equations above needs to be rearranged and combined. Therefor equations (4.2) and (4.3) can be set equal, since in both cases the input measurements $\sigma^0(\mathrm{M25})$ are the same:

$$\frac{m_s(\mathrm{M25},\mathrm{E25})}{100}\cdot \mathrm{sens}(\mathrm{E50}) + \sigma^0_{\mathrm{dry}}(\mathrm{E50}) = \frac{m_s(\mathrm{M25},\mathrm{M25})}{100}\cdot \mathrm{sens}(\mathrm{M25}) + \sigma^0_{\mathrm{dry}}(\mathrm{M25})\,. \tag{4.5}$$

The next steps are rather straightforward to rearrange the equation (4.5) to:

$$m_s(\mathrm{M25},\mathrm{E50}) = m_s(\mathrm{M25},\mathrm{M25})\cdot\frac{\mathrm{sens}(\mathrm{M25})}{\mathrm{sens}(\mathrm{E50})} + \frac{\sigma^0_{\mathrm{dry}}(\mathrm{M25}) - \sigma^0_{\mathrm{dry}}(\mathrm{E50})}{\mathrm{sens}(\mathrm{E50})}\cdot 100\,. \tag{4.6}$$

This new representation of $m_s(\mathrm{M25},\mathrm{E50})$ can be used as substitution in equation (4.4). Hence, another formulation of equation (4.4) looks like:

$$\Delta m_s^{\mathrm{CAL+RES}} = m_s(\mathrm{M25},\mathrm{M25})\cdot\left(\frac{\mathrm{sens}(\mathrm{M25})}{\mathrm{sens}(\mathrm{E50})} - 1\right) + \frac{\sigma^0_{\mathrm{dry}}(\mathrm{M25}) - \sigma^0_{\mathrm{dry}}(\mathrm{E50})}{\mathrm{sens}(\mathrm{E50})}\cdot 100\,. \tag{4.7}$$

The big advantage of the new notation above is now, that it is only dependent on $m_s(\mathrm{M25},\mathrm{M25})$, which can be used to simulated different soil moisture conditions and their impact on Δm_s. The only handicap is that this representation cannot differentiated between the respective dominant cause, either absolute calibration (CAL) or rather spatial resolution (RES). Therefore, a further step is necessary, which will be described in the next section 4.2.

4.2 Splitting resolution- and absolute calibration-related effects

In order to exclude absolute calibration differences, only data from the same instrument has to be used. Therefore, a simple replacement of the model parameters in the last equation (4.7) allows to simulate only the impact of the spatial resolution. The ERS-1/2 model parameters are replaced by the METOP-A model parameters in the same spatial resolution of 50 km. This new notation looks like:

$$\Delta m_s^{\mathrm{RES}} = m_s(\mathrm{M25},\mathrm{M25}) \cdot \left(\frac{\mathrm{sens(M25)}}{\mathrm{sens(M50)}} - 1 \right) + \frac{\sigma^0_{\mathrm{dry}}(\mathrm{M25}) - \sigma^0_{\mathrm{dry}}(\mathrm{M50})}{\mathrm{sens(M50)}} \cdot 100\,, \tag{4.8}$$

which now offers valuable clues about the impact of the resolution mismatch. It can already be predicted that regions with sharp backscatter transitions and a low sensitivity will be mostly affected. The last step to obtain also the impact of the absolute calibration difference is a simple subtraction between equation (4.7) and (4.8). Now it is possible to investigate the occurrence and magnitude of both effects separately.

$$\Delta m_s^{\mathrm{CAL}} = \Delta m_s^{\mathrm{CAL+RES}} - \Delta m_s^{\mathrm{RES}}\,. \tag{4.9}$$

4.3 Availability of model parameters

Of course, the model presented in this chapter needs input data to generate results and proof its validity. The required model parameters are obtained by the offline processor WARP. Within WARP 5.0 approximately 15 years of ERS-1/2 data between 1992-2000 and 2003-2007 were used to generate the model parameters. The first model parameters for METOP-A were derived from scatterometer data between 2007-2008 with WARP 5.2 and are currently in use in the offline regime for extending the surface soil moisture time series.

As already described in previous chapter 3, model parameters are important co-products, which are required for normalisation, error propagation and the final soil moisture retrieval. Without them, a computation of surface soil moisture would not be possible. Unfortunately, the calculation of these model parameters is very costly in terms of processing time. This is also the reason why in the offline regime in WARP 5.2 only ASCAT model parameters were calculated for the higher resolution product. Thus, 50 km model parameters from ASCAT are not available, but would be needed within the model to simulate the artefacts.

An approach to avoid this problem would be to generate 50 km model parameters indirectly out of the 25 km ones. Since in the ground processing at EUMETSAT a Hamming window function is used to achieve the wanted spatial resolution, this suggests to use again a Hamming window function to expand the resolution of the model parameters to 50 km. Therefore, a Hamming window function of the form:

$$H(x) = 0.54 + 0.46 \cos \frac{2\pi x}{a} \quad \text{with} \quad x \leq \left| \frac{a}{2} \right| , \tag{4.10}$$

is used to change the spatial resolution and retrieve the required model parameters indirectly. The correct way of determining the width a of the Hamming window is to deconvolute the Hamming window used in the preprocessing with the desired Hamming window generating a resolution of 50 km. But strictly speaking, the width of the Hamming window function used in the preprocessing at EUMETSAT for the higher resolution product is varying across the swath for the different beams, which generates a spatial resolution ranging from 25 km to 34 km. Therefor a strict solution isn't possible. Thus, the needed width a for the Hamming window function to transform the ASCAT model parameters into 50 km resolution can only be estimated. According to that, the width a was chosen to achieve almost 50 km resolution for all various hamming window sizes already used in the preprocessing.

All available model parameters are summarised in the table 4.1 below:

Model Parameter	**Available**	**Processor**	**Input data of the Processor**
σ^0_{dry}(E50)	Yes	WARP 5.0	ERS-1/2 (1992-2001 & 2003-2007)
σ^0_{wet}(E50)	Yes	WARP 5.0	ERS-1/2 (1992-2001 & 2003-2007)
σ^0_{dry}(M25)	Yes	WARP 5.2	METOP-A (2007-2008)
σ^0_{wet}(M25)	Yes	WARP 5.2	METOP-A (2007-2008)
σ^0_{dry}(M50)	Yes	-	Calculated from σ^0_{dry}(M25)
σ^0_{wet}(M50)	Yes	-	Calculated from σ^0_{wet}(M25)

Table 4.1: Available model parameters.

Chapter 5

Results and Discussion

The upcoming sections will present the results obtained by the model derived in the previous chapter 4. It is applied on the whole globe to get a comprehensive overview of the effected target areas. Consequently, the model is also calculated for regions where the TU-Wien soil moisture algorithm can not or hardly retrieve soil moisture information, e.g. in areas with dense vegetation like tropical forest. The results are in the first place dependent on the model parameters and the form of the model equation. Thus, to draw any conclusion from the graphics directly in the beginning, a discussion on the model characteristics should help for the interpretation.

Subsequently global maps will be presented showing the outcome of the model, as well as a further closer look on Europe and North Africa. Moreover, some statistics were derived for the results, modeled at different soil moisture conditions.

A concluding comparison between the simulated deviations by the model and the estimated soil moisture noise should give information if the results are still below or already beyond the estimated noise level.

5.1 Model considerations and characteristics

Only dry and wet reference are relevant parameters in the model equation (4.7). These are in principle both time-dependent, whereas only the dry reference is changing during the year to account for the vegetation phenology cycle. Thus, the model would give different results during a year. In this respect, only the maximum calibration-related impact will be determined, which will be expected to occur when the sensitivity is at its lowest level or in other words the dry reference is at its maximum level. Of course, the day in question will not be overall the same, since it is dependent on the climate zone and land cover when the dry reference is at its maximum.

A general notation of the derived model in the last chapter will look like:

$$\Delta m_s(x,y,m_s) = \underbrace{\left(\frac{\sigma^0_{sens}(x)}{\sigma^0_{sens}(y)} - 1\right)}_{k} \cdot m_s + \underbrace{\left(\frac{\sigma^0_{dry}(x) - \sigma^0_{dry}(y)}{\sigma^0_{sens}(y)} \cdot 100\right)}_{d}, \tag{5.1}$$

which represents a linear equation with slope k and intercept d. Both shape parameters, k and d respectively, are represented by model parameters. The parameter m_s is used to simulate different soil moisture conditions and can therefore vary between 0 and 100%. Now its apparently visible why the maximum effect can be expected at the lowest sensitivity, since it acts like an attenuation at the slope and intercept parameter. Figure 5.1 shows equation (5.1) in a graphical manner.

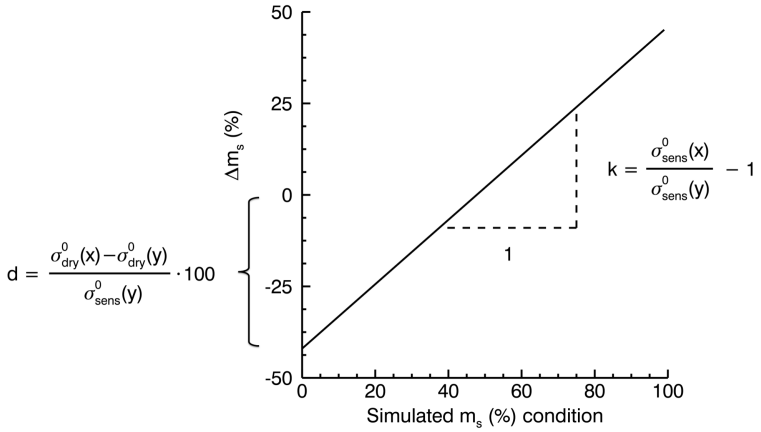

Figure 5.1: Equation (5.1) in a graphical manner.

A big slope k will illustrate that either one or both references differ enormously, whereas a small slope indicates that the scaling range is rather similar. A steep incline may arise from different environmental conditions captured within the period covered by the input data. For example, this would include an abnormally long-lasting drought or flood, since ASCAT model parameters are derived from 2 years only, whereas model parameters derived from 15 years ERS-1/2 scatterometer data will be more robust in this respect. Such results might be delimited on certain areas and needs to be further investigated by additional datasets to prove this assumption.

The occurrence of the intercept d is only dependent on a mismatch of the dry references. Already small differences can have a big impact just because of a rather small sensitivity in a certain area. Thus, a big intercept needs to be assessed carefully regarding the sensitivity.

In case of dry soil conditions ($m_s = 0$) the equation (5.1) will result into:

$$\Delta m_s(x, y, 0) = \underbrace{\left(\frac{\sigma^0_{\text{dry}}(x) - \sigma^0_{\text{dry}}(y)}{\sigma^0_{\text{sens}}(y)} \cdot 100 \right)}_{d}. \tag{5.2}$$

Thus, only the intercept parameter d remains, that is now controlling the deviation parameter Δm_s. The result could be either a negative or positive number depending on which dry reference is lower. For example, a difference of ± 0.5 dB for the dry references together with a sensitivity of 5 dB will yield to a deviation of $\pm 20\%$.

Since the model will be applied on each DGG point separately, every point has its own slope and intercept value. As a result the deviation will change differently on a soil moisture increase or decrease at each point. Thus, an increase of soil moisture could either have a positive, negative or almost no effect on the deviation.

Since the model will be split up into the two expected major causes, the description of the linear equation is valid for both cases. This would mean both effects together are actually a superposition of two lines, one specifying the characteristics of absolute calibration and the other one the influence of the resolution mismatch.

5.2 Simulating calibration-related artefacts

The first results are based on equation (4.7), where all effects are presence and the full impact is modeled. This case is further denoted as "BOTH" in the Figures, since the expected two major causes are not separated. Figure 5.2 shows the statistics derived from all DGG points for three different soil moisture conditions: 0%, 50% and 100%. In the box-plot on the left, the height of the box illustrated the interquartile range (IQR), whereas the whiskers show the maximum data within $Q_1 - (1.5 \times \text{IQR})$ and $Q_3 + (1.5 \times \text{IQR})$. Mild outliers, between the whisker ends and $< 3 \times \text{IQR}$, are indicated as crosses. Unfortunately they are not easily distinguishable, since there are so many that they overlay each other. Extreme outliers ($> 3 \times$ IQR) are masked out within the statistics. The two other graphics on the right show the distribution of the results in a relative cumulative frequency plot and histogram. Negative values can be interpreted as an underestimation of soil moisture in the initial ASCAT soil moisture product. And if the results are positive it is exactly inverted, which means that soil moisture has been overestimated by the ERS-1/2 model parameters. The important information from the statistics is that an overestimation is throughout visible, but with increasing soil moisture the deviation gradually decreases. Thus, in general a higher soil moisture condition has a positive impact, which reduces the calibration-related artefacts.

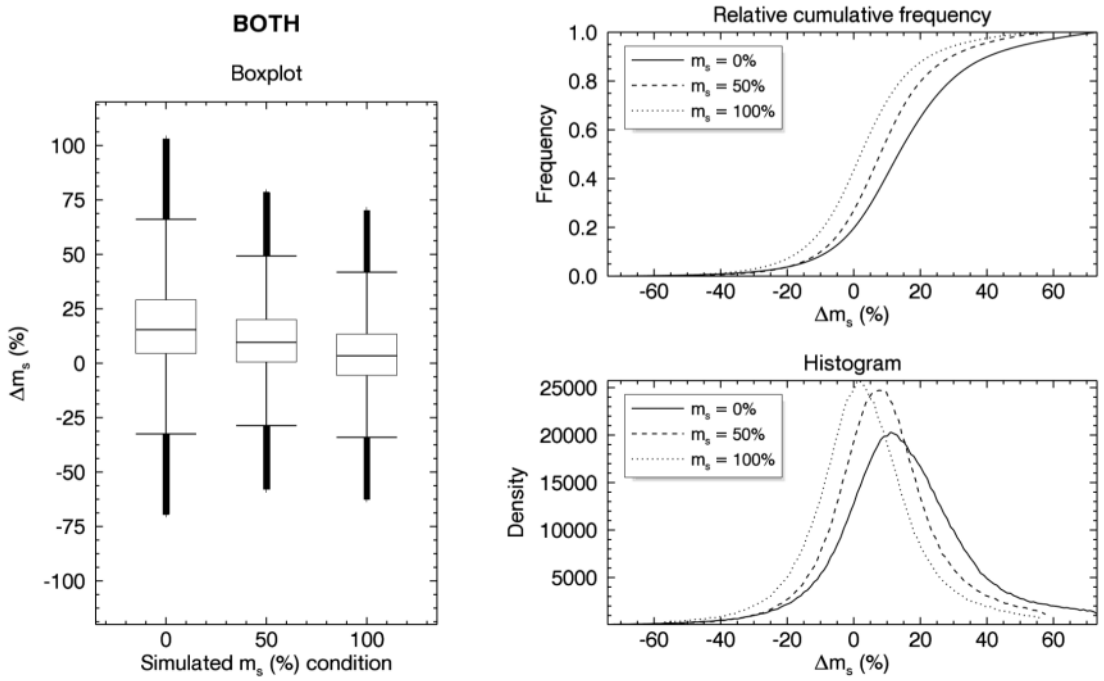

Figure 5.2: Statistics derived from the deviations originated by all calibration-related differences.

The next Figure 5.3 shows three global maps with the deviations obtained by the model simulated for three different soil moisture conditions. Now it is important to remember the sensitivity to soil moisture (Figure 3.7-b) to interpret the results in the right way. The dark blue areas especially in Figure 5.3-a and 5.3-b around the latitudes ±5° are in the first place related to the low sensitivity in these regions. But anyhow, the soil moisture retrieval does not perform very well in those regions due to the dense vegetation there. Europe shows a rather strong positive deviation, which might be also related to a small sensitivity in these area. Australia is the only continent which has rather low deviations compared to the others. Furthermore, the gradually decrease of the deviations with increasing soil moisture, which has been already seen in the statistics, is observable in the global maps as well.

A closer look on Europe and North Africa is illustrated in Figure 5.4 simulated for a complete dry and wet soil. The visible artefacts in the initial ASCAT soil moisture product are highlighted very well, especially in areas with topographic complexity, e.g. in the south of Algeria or Libya. But also cities in Europe stick out as small circles like in the initial ASCAT product. Thus, the model declares a continually overestimation of urban areas, whereas topographic features alter between over- and underestimation.

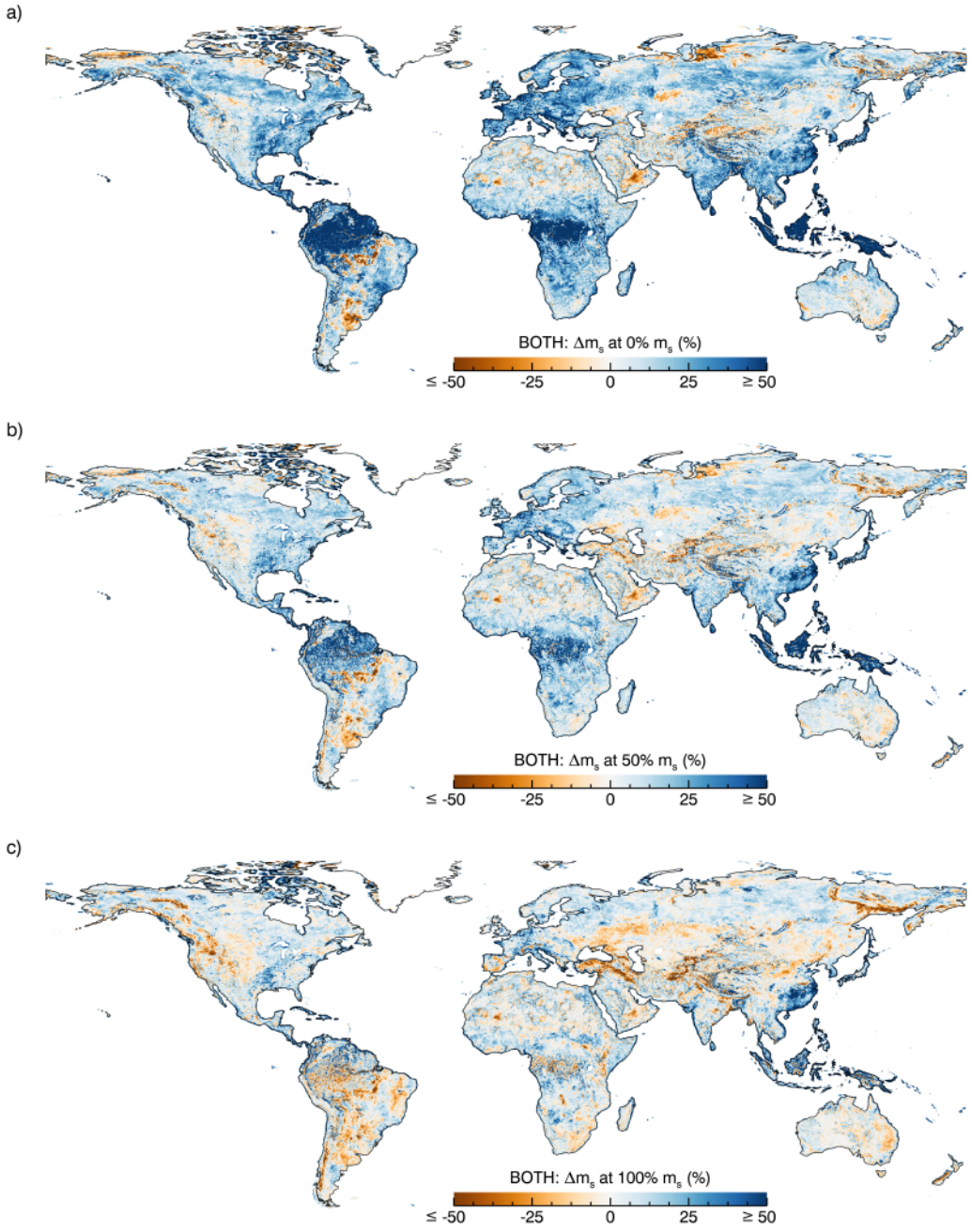

Figure 5.3: Global maps illustrating the total calibration-related modeled deviations for 0% *(a),* 50% *(b) and* 100% *(c) soil moisture.*

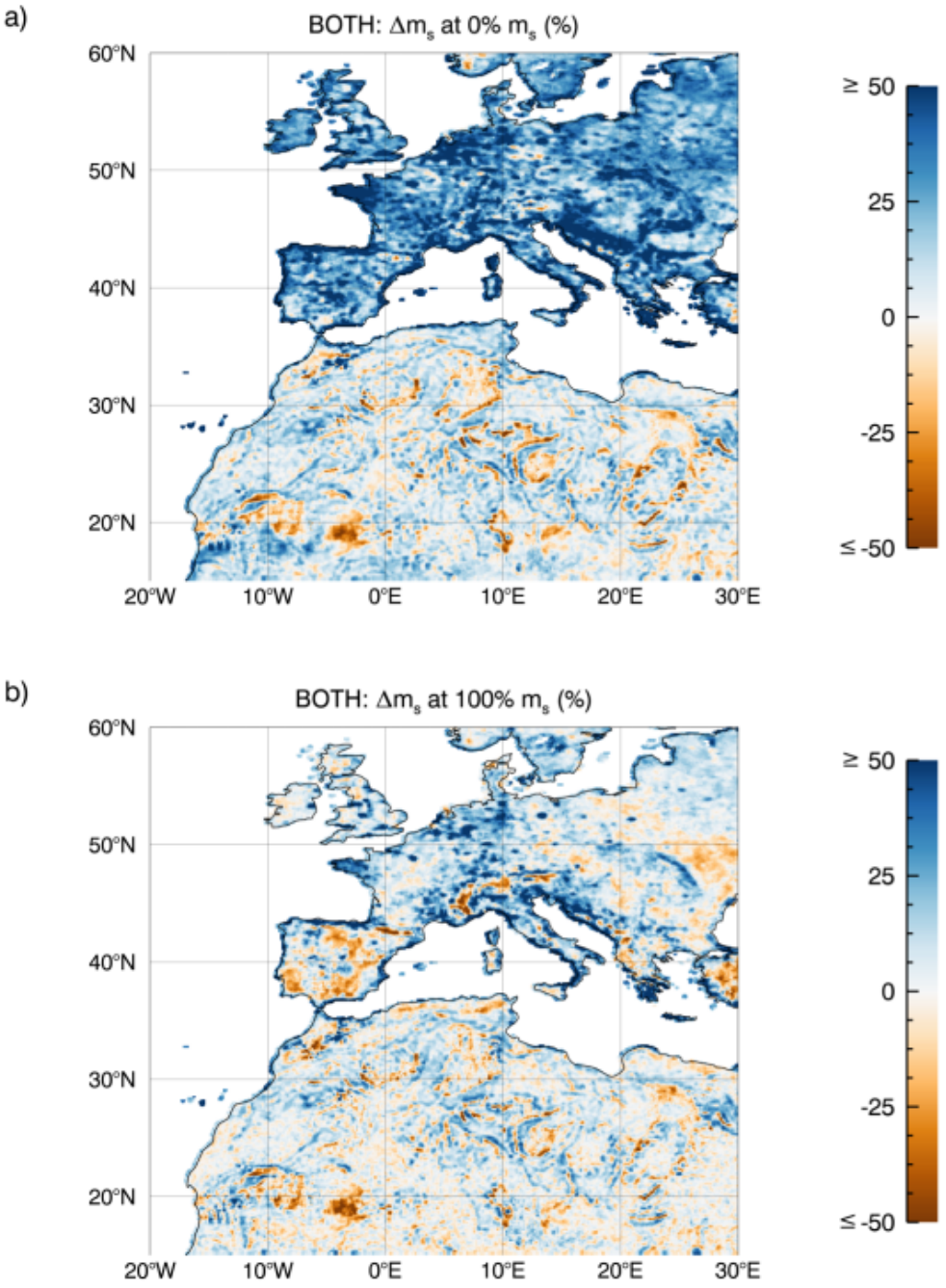

Figure 5.4: A closer look on Europe and North Africa showing the deviations coming from the total calibration-related mismatch. Once for a dry (a) and wet soil (b).

5.3 Consequences of the resolution mismatch

The soil moisture deviation arising from a resolution mismatch can be modeled by equation (4.8). Statistics derived from those results are presented in Figure 5.5. The box-plot shows again the interquartile range, whereas the whiskers show the maximum data below ($\pm 1.5 \times$ IQR). The impact due to the resolution mismatch is rather low ($\pm 6\%$ for 50% of the points) and a decrease of the deviations with increasing soil moisture is also here visible. However, interesting is that the uniformly distributed histogram is not directly centered over zero, but slightly shifted to -1.5%. Thus, a mismatch of the resolution would rather tend to an overall underestimation of soil moisture in the initial ASCAT soil moisture product.

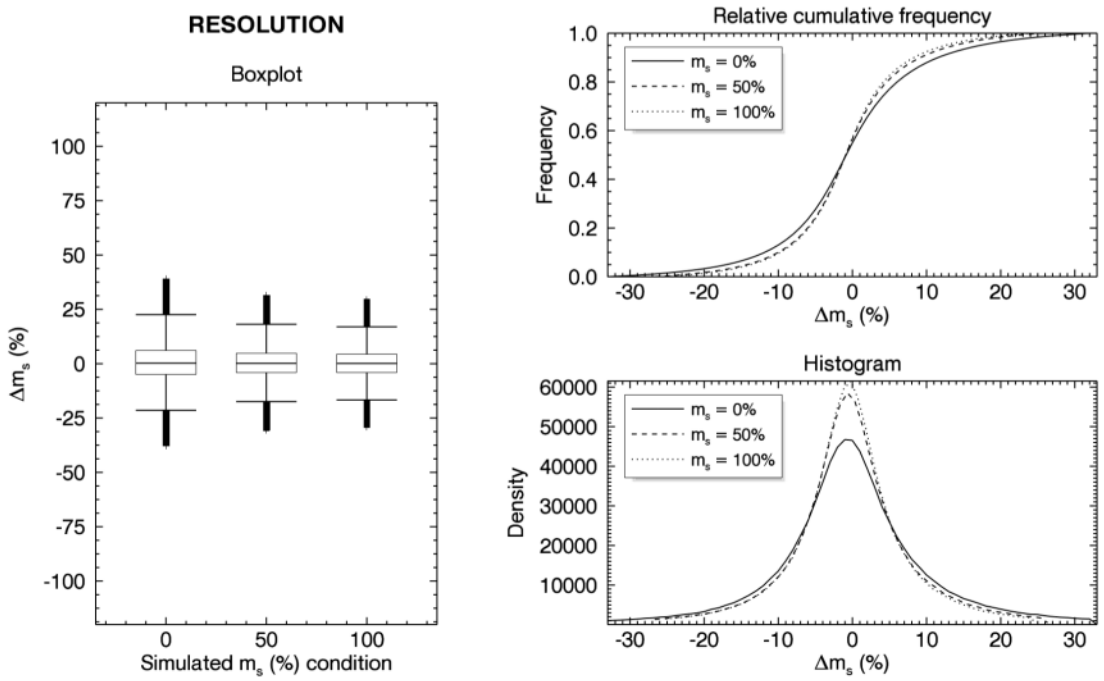

Figure 5.5: Statistics derived from deviations arising by a resolution mismatch.

Three global maps are illustrated in the Figure 5.6. Again, each simulated with different soil moisture conditions. As already expected, areas with sharp backscatter changes are mostly affected. Such regions include: mountainous areas, cities, tropical forests and areas around small lakes. A steadily decrease of the deviations with increasing soil moisture is hardly visible in the global maps, but can be observed on a smaller scale over Europe and North Africa (see Figure 5.7). Cities and areas with topographic complexity are really highlighted with dark colors, but some features disappear with increasing soil moisture conditions. Overall the soil moisture deviations arising from a resolution mismatch are rather low.

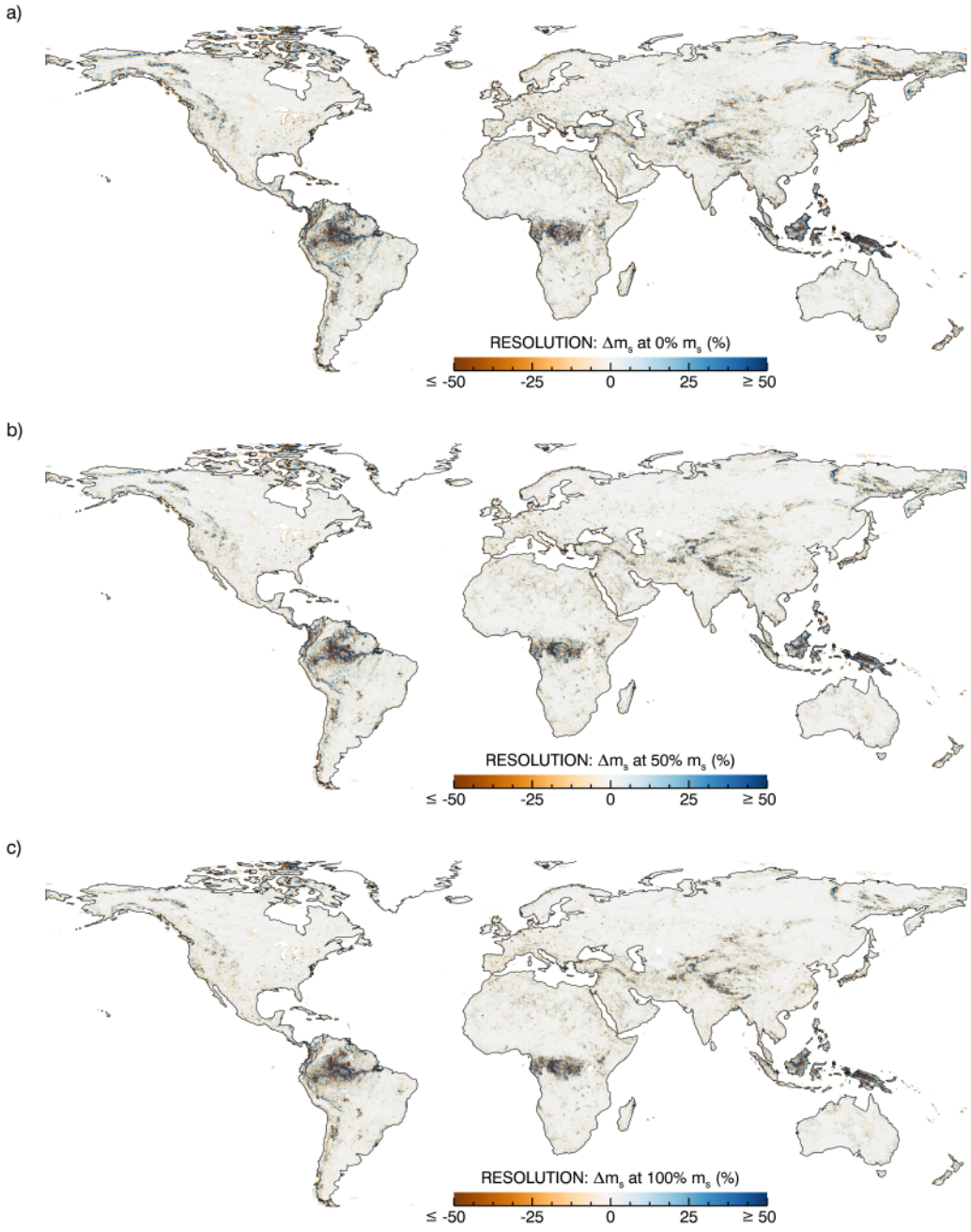

Figure 5.6: Simulated deviations as a consequence of a resolution mismatch on global maps for three different soil moisture conditions: 0% *(a),* 50% *(b) and* 100% *(c).*

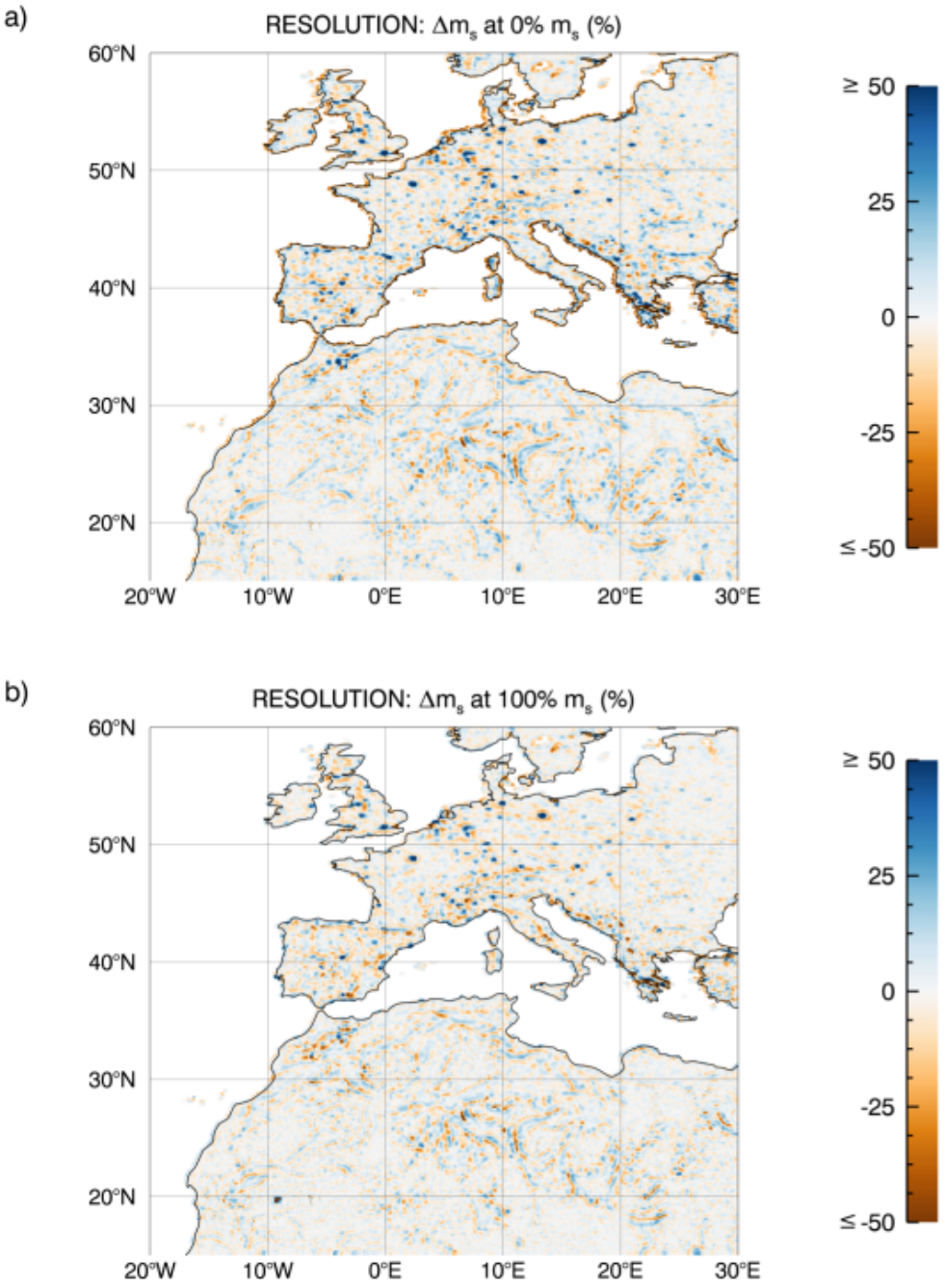

Figure 5.7: A closer look on Europe and North Africa showing the deviations arising by a resolution mismatch. Once for a dry (a) and wet soil (b).

5.4 Impact of absolute calibration differences

The quantification of the possible presence of an absolute calibration difference can be obtained by equation (4.9). It is simply a difference between the last two simulated situations. Again, the same statistical graphics have been computed and are presented in Figure 5.8. The box-plot on the left shows that most of the deviations are positive for dry conditions, but with increasing soil moisture deviations are getting less. Thus, the expected behaviour of overestimation can be seen only in case of low soil moisture, whereby an increase of soil moisture acts against these characteristics.

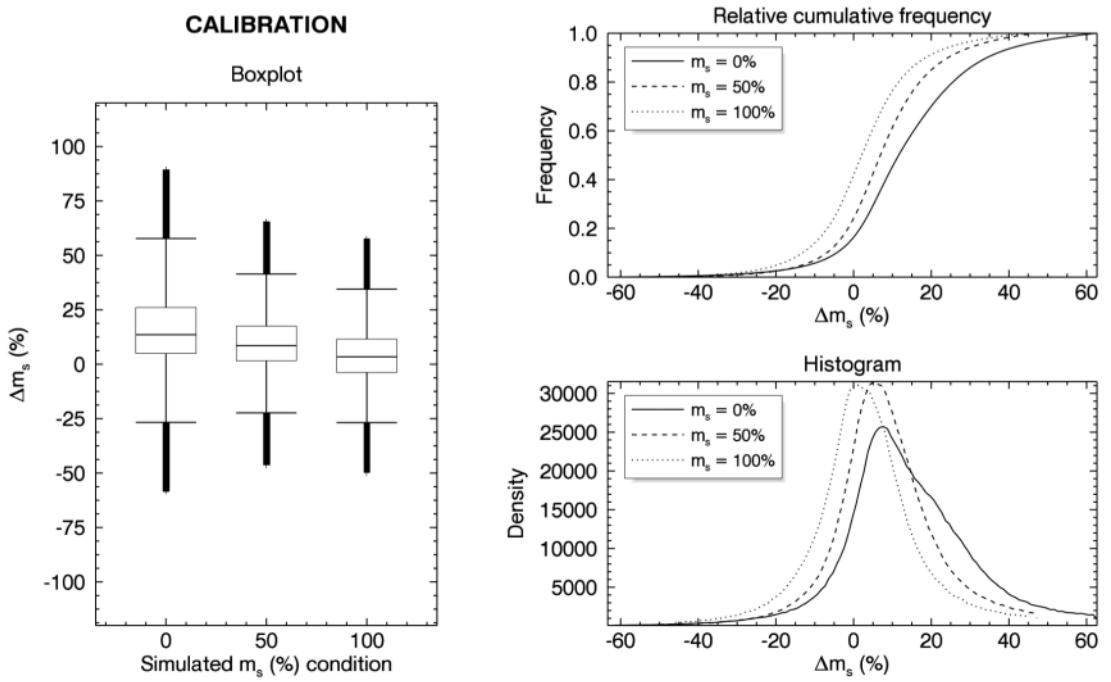

Figure 5.8: Statistics derived from simulated deviations arising by an absolute-calibration difference.

Again, three global maps (Figure 5.9), as well as a zoom on Europe and North Africa (Figure 5.10) have been generated. However, to get an idea of how an absolute calibration difference of, for example 0.22 dB, will be afflicted in the results, can be seen in Figure 5.11. This global map demonstrates the expected deviations and matches very well to the statistics shown in the box-plot in Figure 5.8 in case of 0% soil moisture. Soil moisture is overestimated all over the world with respect to the sensitivity at each location. Similarities can be also found in Figure 5.9-a, but there are also some spots which show complete different behaviour.

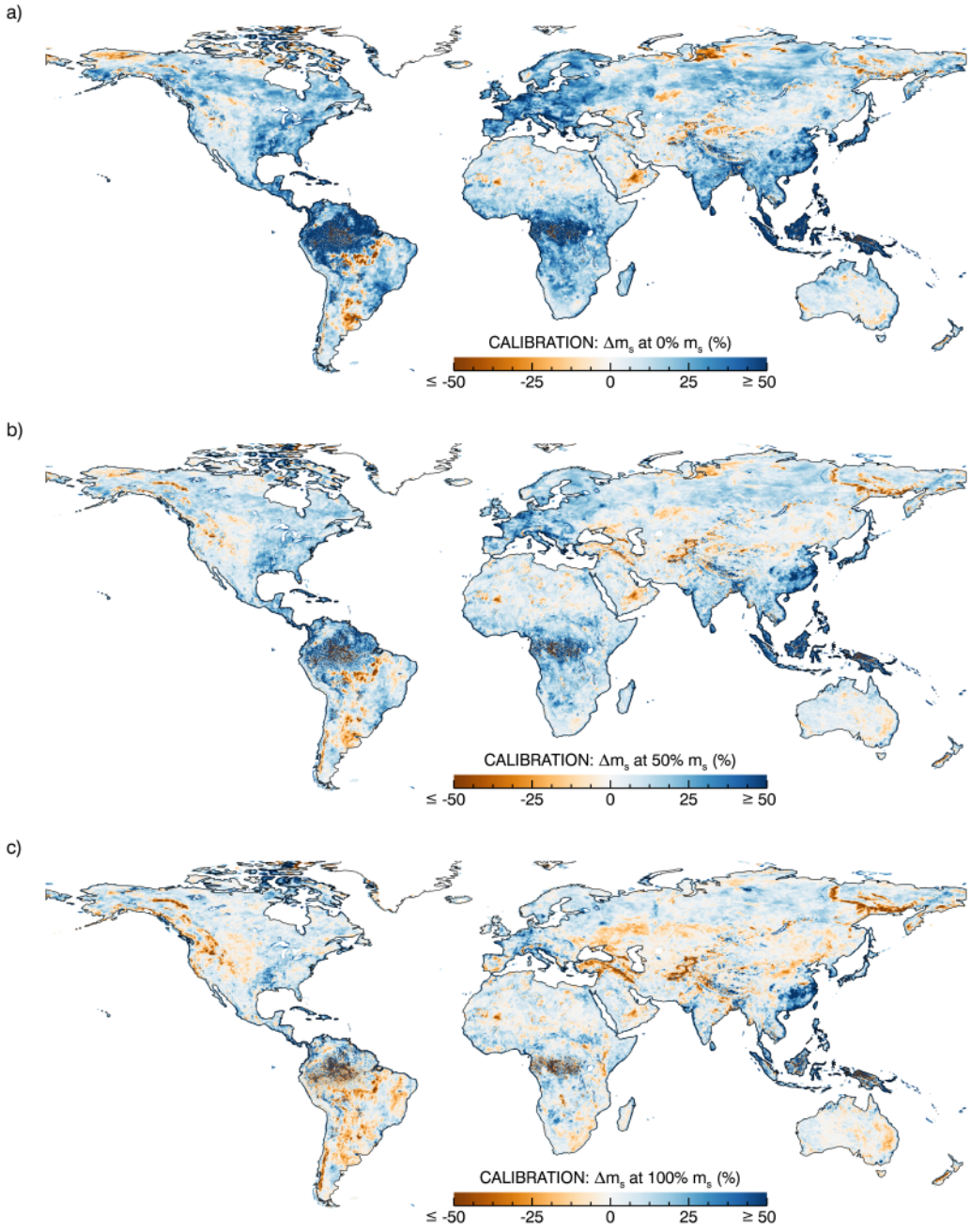

Figure 5.9: Simulated deviations as a consequence of an absolute calibration difference on global maps for three different soil moisture conditions: 0% *(a),* 50% *(b) and* 100% *(c).*

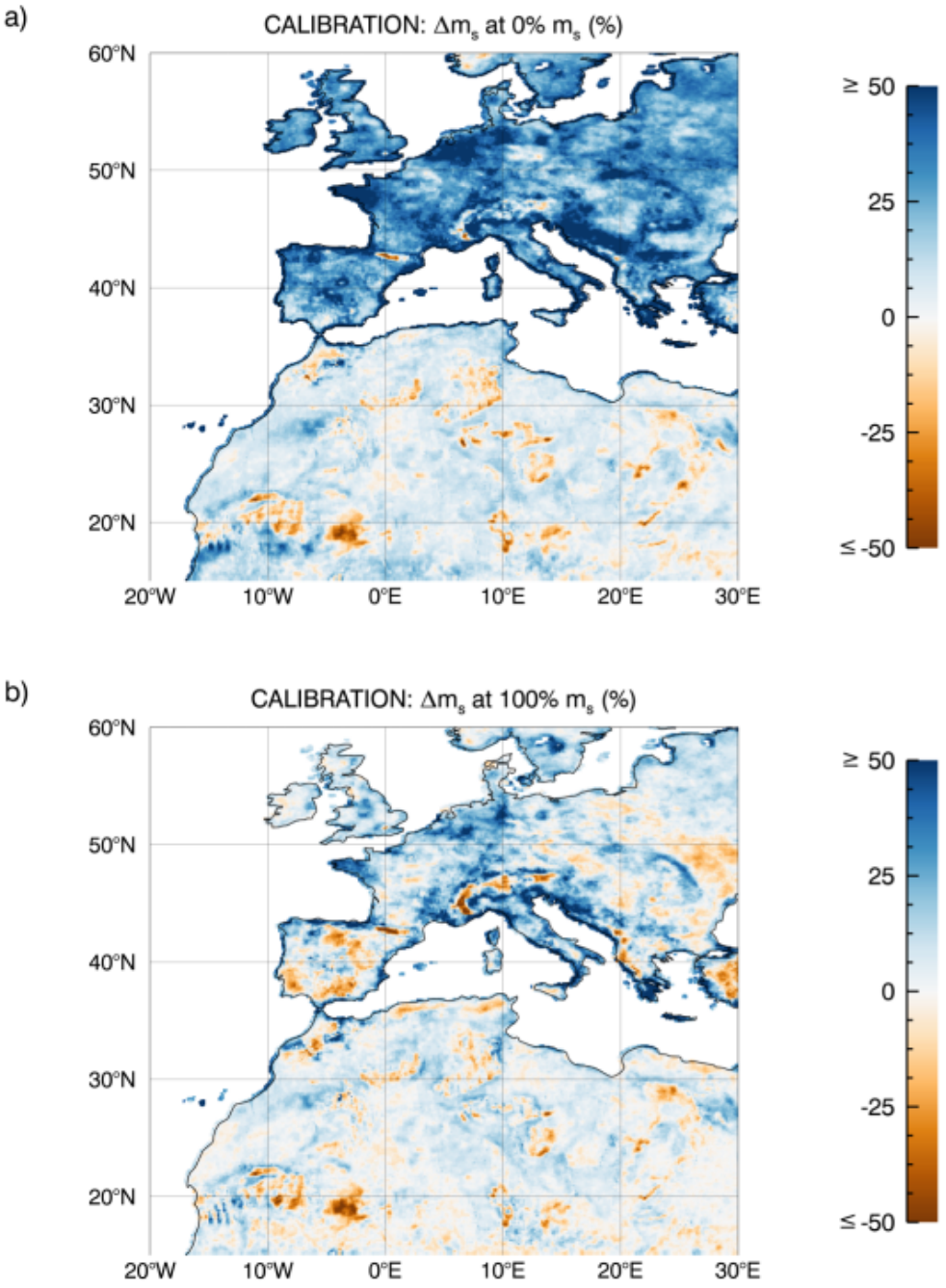

Figure 5.10: A closer look on Europe and North Africa showing the deviations coming from an absolute calibration difference. Once for a dry (a) and wet soil (b).

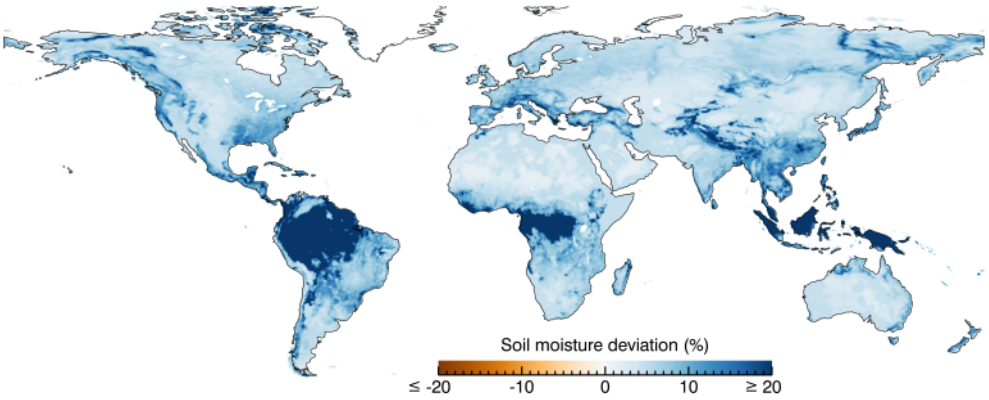

Figure 5.11: The impact on soil moisture with a simulated bias of 0.22 *dB*.

One interesting spot is located in Argentina, South America. As already mentioned, the METOP-A model parameters are based on 2007 and 2008, whereas the ERS-1/2 model parameters on more than 15 years and thus are more robust in this respect. However, Argentina has had its worst drought since decades in the end of 2008 and beginning of 2009 (*Piette*, 2009). Therefore, the derived dry reference from METOP-A scatterometer data is much lower compared to ERS-1/2. The pattern of the mismatch (see Figure 5.12) corresponds very well to a vegetation index anomaly image derived from the Moderate Resolution Imaging Spectroradiometer (MODIS) on NASA's Terra satellite (see Figure 5.13). Thus, in this case the deviation is really related to an abnormally drought. This would actually mean that 2 years of model parameters could be very "noisy" or in other words not robust against extreme environmental conditions. Another example would be Europe in Figure 5.10-a. The deviations are constantly positive over Europe, which would indicate that Europe has not been as dry in 2007-2008 compared to 1992-2007. But such a statement needs to be proven by additional datasets, because the presence of an absolute calibration difference could also be responsible in this case.

A conclusion to the presented results in this chapter so far is that the deviation arising by a resolution mismatch has been simulated as expected, whereas deviations coming from an absolute calibration difference were noticeable but disturbed by unstable model parameters. An interesting aspect is that the deviations will get lower with increasing soil moisture. Such an observation must be the result of closer wet references than dry references. But it is important to remember that the dry reference will change during the year according the vegetation phenology circle, whereas the wet reference stays constant. Therefore, the chance that the dry reference will differ more easily is much higher than compared to the wet reference.

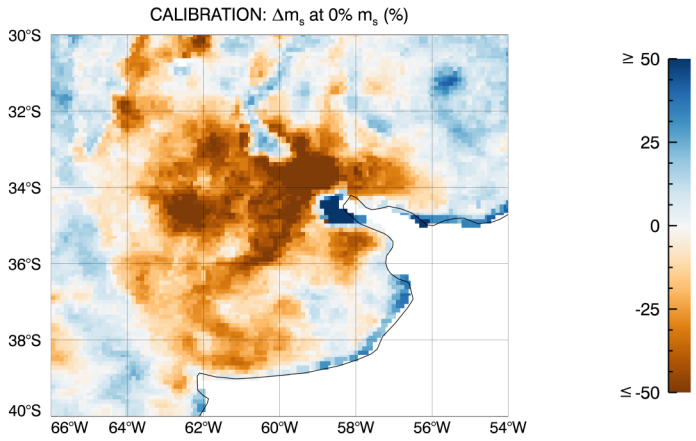

Figure 5.12: Simulated deviations due to an absolute calibration difference for dry conditions in Argentina, South America. In this case the modeled deviations are related to an abnormally drought caught by METOP-A in December 2008.

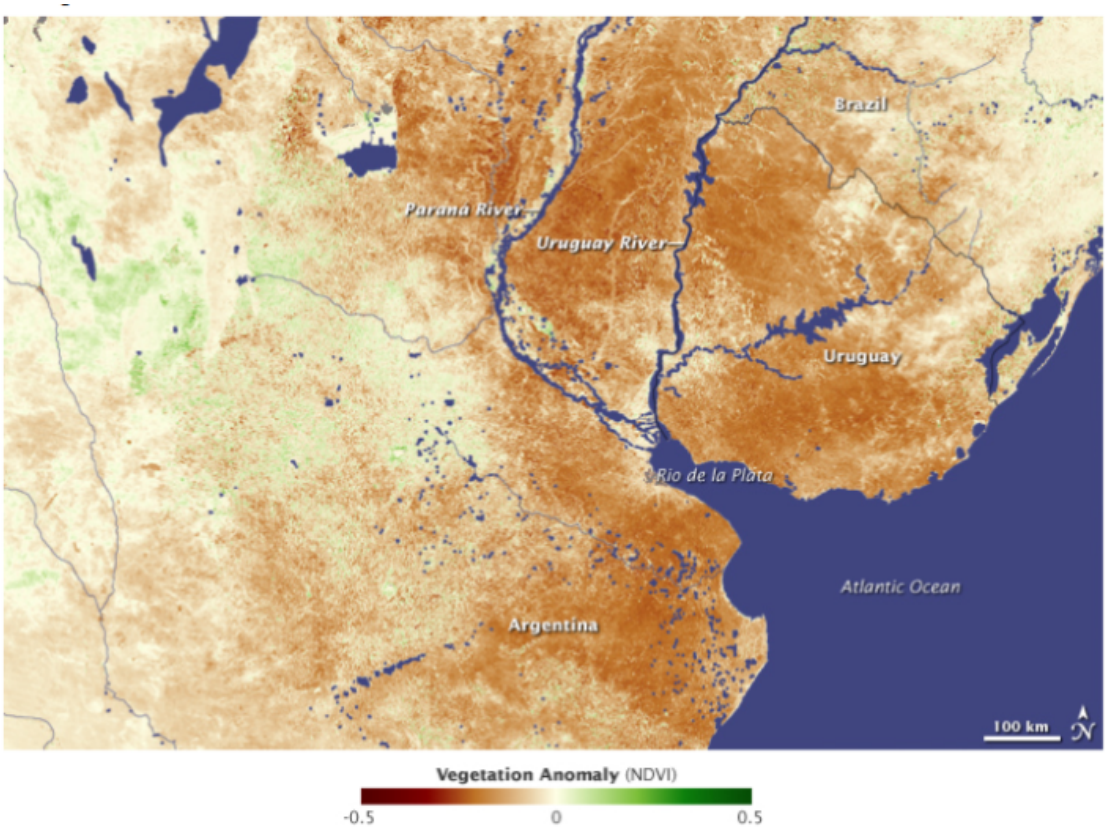

Figure 5.13: Vegetation index anomaly derived from MODIS on NASA's Terra satellite for January 17 - February 1, 2009 (NASA Earth Observatory, 2011).

5.5 Comparison to soil moisture noise

In the end it is important to know if these simulated deviations are still below the soil moisture noise level or already beyond it. In the WARP 5.2 error model the soil moisture noise is calculated for each day per point. For further analysis only the maximum noise for each point has been evaluated and compared to the previous results. Figure 5.14 shows a global map of the maximum soil moisture noise.

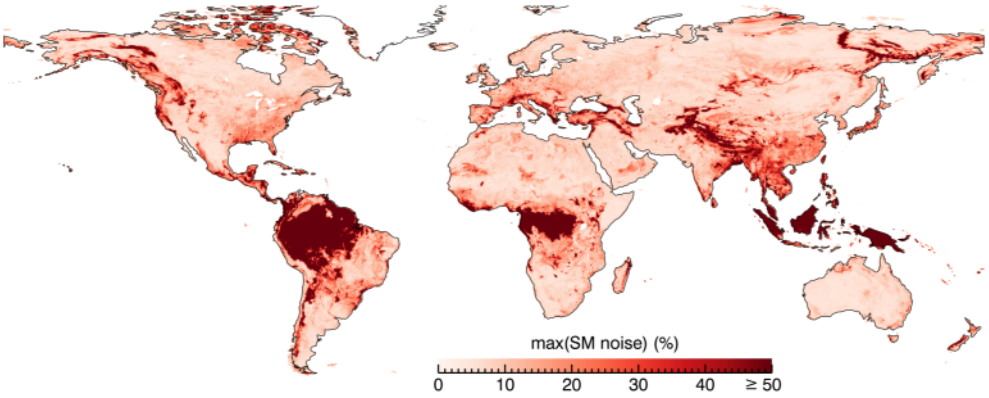

Figure 5.14: Maximum soil moisture noise.

It has been analysed which points are always below or above the maximum noise level and which points are in dependency on the soil moisture conditions once below or above the noise level. The deviations generated by a resolution mismatch (Figure 5.15-a) will be overall below the maximum soil moisture noise, only in dedicated regions they are above or are actually depending on the soil moisture condition. The simulated deviations due to an absolute calibration difference (Figure 5.15-b) has a considerably greater fraction of points which will be below or above the noise level according to the prevailing soil moisture conditions. Also the number of points which will be always above the noise level is remarkably increased. If both effects are examined together, it can be observed that sometimes the two effects amplify or damp each other. An amplification is clearly visible in case of Australia and Africa.

A conclusion of this analysis is that a resolution mismatch will not raise soil moisture significantly above the maximum soil moisture noise level. Blue and especially red areas in case of the comparison between the maximum noise level and the modeled deviations as a consequence of an absolute calibration difference would need further investigation in order to check if these results are due to differences from an abnormally event afflicted in the dry or wet reference of METOP-A.

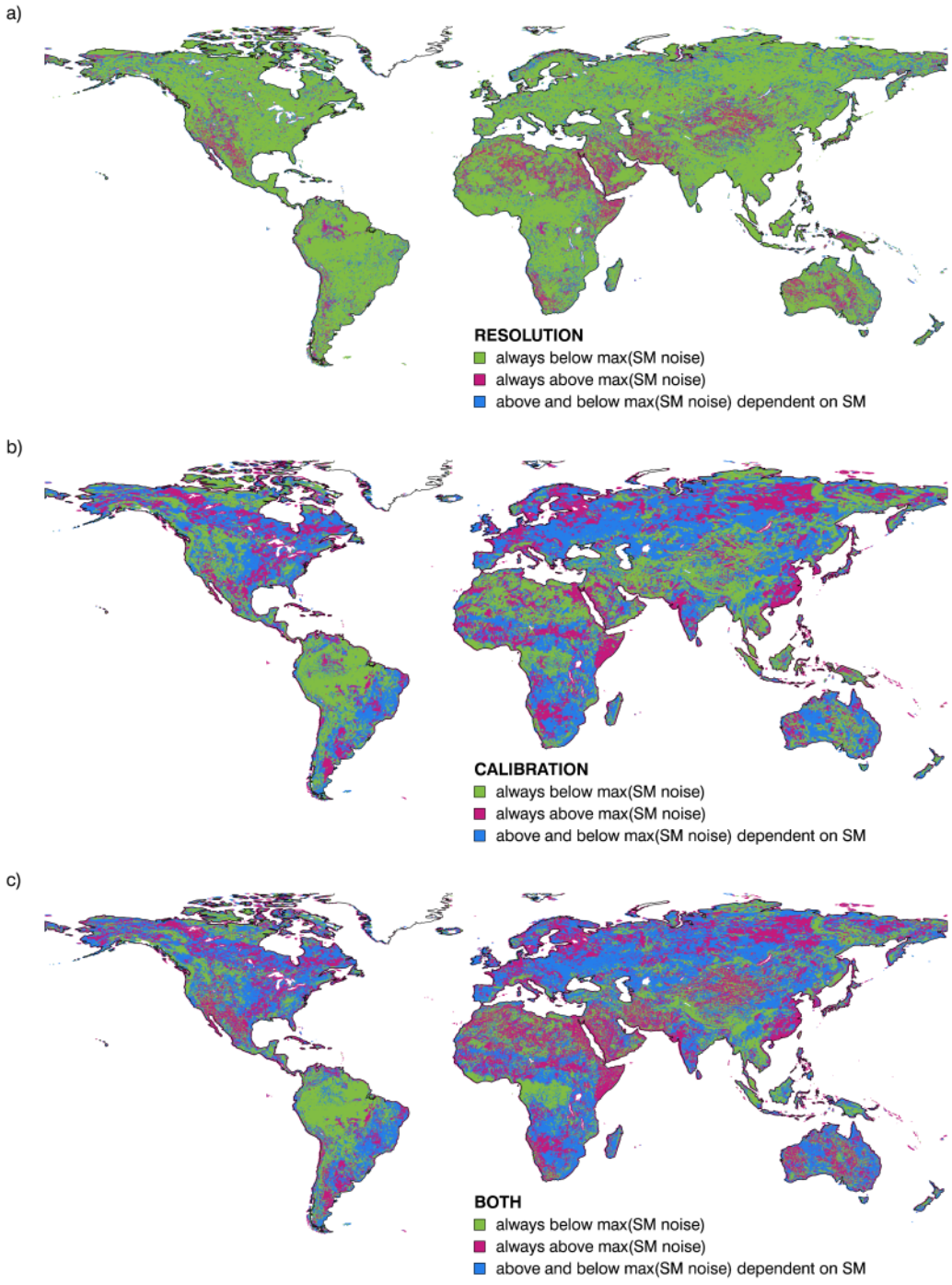

Figure 5.15: A comparison of the simulated deviations to the maximum soil moisture noise for a resolution mismatch (a), an absolute calibration difference (b) and both effects together (c).

Chapter 6

Summary and Outlook

The presented study has started with an attempt to highlight similarities between a nominal product life cycle and products derived from satellites. This common introduction should emphasis the initial state of the ASCAT soil moisture product, where the model parameters in the WARP NRT processor have not been updated so far. Hence, the processor is still using ERS-1/2 model parameters derived from approximately 15 years. The aggregation of ASCAT backscatter measurements and ERS-1/2 model parameters in the NRT processor induce soil moisture artefacts due to a calibration-related mismatch. It was planned to update the model parameters as soon as ERS-2 scatterometer data has been reprocessed to 25 km resolution and a new model parameters based on ERS-2 and METOP-A could have been derived. The reprocessing is still pending and therefore the ASCAT soil moisture product also remains in its initial state.

This ongoing interim solution has motivated this study to investigate the artefacts which are visible in the initial ASCAT soil moisture product. It turned out that a simple model is able to simulate the artefacts arising by a resolution mismatch. In case of an absolute calibration difference only for low soil moisture conditions the expected behaviour of an overestimation has been exposed. The global maps showed regions with different characteristics, which might be due to unstable model parameters derived from 2 years of METOP-A. Thus, once model parameters were derived from a longer acquisition period such characteristics might disappear. Another way to display only the impact of an absolute calibration difference would be to focus on stable backscatter targets or to go even back to the Level 1 data, as actually planned.

Further research activities are planned on inter-calibration of METOP-A and ERS-1/2 scatterometer data, but at first the next update of the model parameters in the initial ASCAT soil moisture product will be based only on ASCAT data itself. First tests have already been started and improvements are clearly visible (see Figure 6.1).

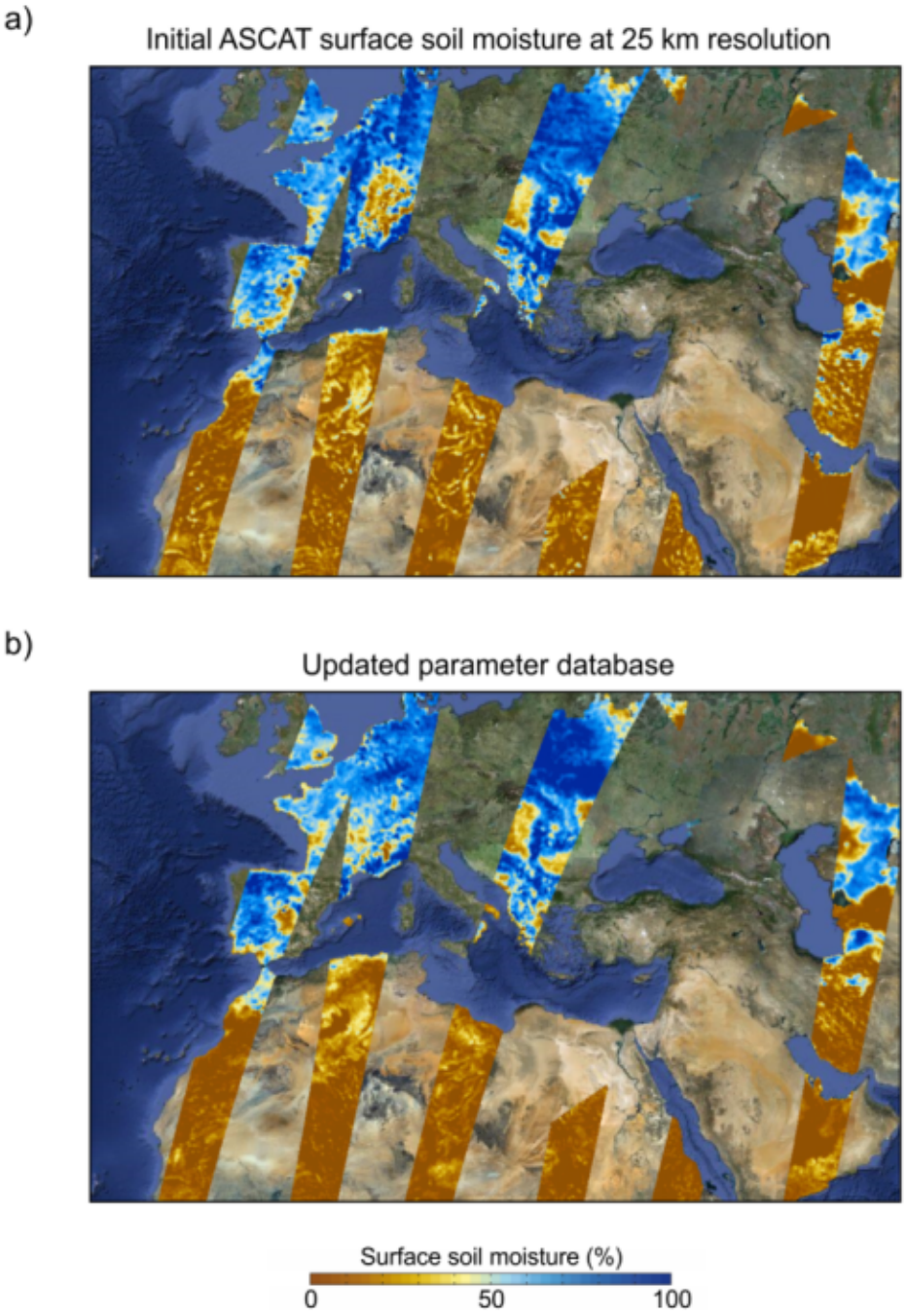

Figure 6.1: The initial ASCAT soil moisture product at 25 km resolution processed with current ERS-1/2 model parameters (a) and first results with updated model parameters based on 2 years of ASCAT (b). Both images show the descending orbit from 2010/03/22 over Europe and North Africa overlayed on Google satellite images.

Bibliography

Bartalis, Z. (2009), Spaceborne Scatterometers for Change Detection over Land, Ph.D. thesis, Vienna University of Technology, Austria, PhD dissertation.

Bartalis, Z., K. Scipal, and W. Wagner (2006a), Azimuthal anisotropy of scatterometer measurements over land, *IEEE Transactions on Geoscience and Remote Sensing*, **44**(8), p. 2083–2092.

Bartalis, Z., R. A. Kidd, and K. Scipal (2006b), Development and implementation of a discrete global grid system for soil moisture retrieval using the MetOp ASCAT scatterometer, in *First EPS/MetOp RAO Workshop*, Frascati, Italy, 15–17 May, ESA Special Publication SP-618.

Bartalis, Z., W. Wagner, V. Naeimi, S. Hasenauer, K. Scipal, H. Bonekamp, J. Figa, and C. Anderson (2007), Initial soil moisture retrievals from the METOP-A Advanced Scatterometer (ASCAT), *Geophysical Research Letters*, **34**(L20401), doi:10.1029/2007GL031088.

Born, G. H., J. A. Dunne, and D. B. Lame (1979), Seasat mission overview, *Science*, **204**(4400), p. 1405–1406.

Ceballos, A., K. Scipal, W. Wagner, and J. Marínez-Fernández (2005), Validation of ERS scatterometer-derived soil moisture data in the central part of the Duero Basin, Spain, *Hydrological Processes*, **19**(8), p. 1549–1566.

CEOS (2010), The earth observation handbook, http://www.eohandbook.com/, accessed on 2010 December 22.

Duchossois, G., and P. Martin (1995), ERS-1 and ERS-2 Tandem Operations, *ESA Bulletin*, **83**.

Duchossois, G., G. Kohlhammer, and P. Martin (1996), Completion of the ERS Tandem Mission, *ESA Earth Observation Quarterly*.

EUMETSAT (2006), An Introduction to the EUMETSAT Polar System, http://www.eumetsat.int/eps_webcast/eps/index.htm, accessed on 2011 February 20.

EUMETSAT (2008), News - ASCAT Level 2 Soil Moisture Operational, http://www.eumetsat.int/Home/Main/News/Features/708786, accessed on 2011 January 28.

EUMETSAT (2009), ASCAT Product Guide, *Tech. rep.*, European Organisation for the Exploitation of Meteorological Satellites, Darmstadt, Germany.

EUMETSAT (2010), Satellite Programmes Overview, http://www.eumetsat.int/Home/Main/Satellites/SatelliteProgrammesOverview/index.htm, accessed on 2010 December 1.

Figa-Saldaña, J., J. J. W. Wilson, E. Attema, R. Gelsthorpe, M. R. Drinkwater, and A. Stoffelen (2002), The advanced scatterometer (ASCAT) on the meteorological operational (MetOp) platform: A follow on for European wind scatterometers, *Canadian Journal of Remote Sensing*, **28**(3), p. 404–412.

Fontaine, B., S. Louvet, and P. Roucou (2007), Fluctuations in annual cycles and inter-seasonal memory in West Africa: rainfall, soil moisture and heat fluxes, *Theoretical and Applied Climatology*, **88**(1–2), p. 57–70.

Gelsthorpe, R. V., E. Schied, and J. J. W. Wilson (2000), ASCAT – Metop's advanced scatterometer, *ESA Bulletin (ISSN 0376-4265)*, **102**, p. 19–27.

Grantham, W., E. Bracalente, W. Jones, and J. Johnson (1977), The seasat-a satellite scatterometer, *Oceanic Engineering, IEEE Journal of*, **2**(2), p. 200 – 206, doi:10.1109/JOE.1977.1145338.

Henderson, F. M., and A. J. Lewis (1998), *Principles and Applications of Imaging Radar*, *Manual of Remote Sensing*, vol. 2, 3rd ed., John Wiley & Sons, New York, USA.

Jordan, A. K., C. G. Purves, and J. F. Diggs (1976), An Analysis of Skylab II S193 Scatterometer Data, *Geoscience Electronics, IEEE Transactions on*, **14**(2), p. 97 –100.

Kidd, R. A. (2005), NWP User Community Requirements Summary, ASCAT Soil Moisture Report Series, No. 1, *Technical Report*, Institute of Photogrammetry and Remote Sensing, Vienna University of Technology, Austria.

Klaes, D., M. Cohen, Y. Buhler, P. Schlüssel, R. Munro, J.-P. Luntama, A. von Engeln, E. Ó'Clérigh, H. Bonekamp, J. Ackermann, and J. Schmetz (2007), An introduction to the EUMETSAT Polar System, *Bulletin of the American Meteorological Society*, **88**(7), p. 1085–1096.

Kottek, M., J. Grieser, C. Beck, B. Rudolf, and F. Rubel (2006), World map of the Köppen-Geiger climate classification updated, *Meteorologische Zeitschrift*, **15**, p. 259–263.

Kramer, H. (2002), *Observation of the earth and its environment: survey of missions and sensors*, 4th ed. ed., Springer.

Lecomte, P., and W. Wagner (1998), ERS Wind Scatterometer commissioning and in-flight calibration, in *ESA/EUMETSAT Workshop: Emerging Scatterometer Applications — From research to operations*, ESTEC, Noordwijk, The Netherlands, 5–7 October.

Naderi, F. M., M. H. Freilich, and D. G. Long (1991), Spaceborne radar measurement of wind velocity over the ocean - An overview of the NSCAT scatterometer system, *Proceedings of the IEEE*, **79**(6), p. 850–866.

Naeimi, V. (2009), Model improvements and error characterization for global ERS and METOP scatterometer soil moisture data, Ph.D. thesis, Vienna University of Technology, Austria, PhD dissertation.

Naeimi, V., Z. Bartalis, and W. Wagner (2009), ASCAT Soil Moisture: An Assessment of the Data Quality and Consistency with the ERS Scatterometer Heritage, *Journal of Hydrometeorology*, **10**, p. 555–563, doi:10.1175/2008JHM1051.1.

NASA Earth Observatory (2011), Drought in Southern South America, http://earthobservatory.nasa.gov/NaturalHazards/view.php?id=37239, accessed on 2011 March 3.

Neyt, X., P. Pettiaux, and M. P. J. Acheroy (2002), Scatterometer ground processing review for gyro-less operations, in *Proceedings of SPIE, Remote Sensing of the Ocean and Sea Ice*, Agia Pelagia, Greece, 23–27 September.

Niederreiter, H. (1992), *Random Number Generation and Quasi-Monte Carlo Methods*, Society for Industrial Mathematics.

NOAA (2011), The Initial Joint Polar-Orbiting Operational Satellite System (IJPS) web site, http://projects.osd.noaa.gov/IJPS/, accessed on 2011 January 22.

Pellarin, T., J.-C. Calvet, and W. Wagner (2006), Evaluation of ERS scatterometer soil moisture products over a half-degree region in southwestern France, *Geophysical Research Letters*, **33**(17), p. Art. No. L17,401, doi:10.1029/2006GL027231.

Piette, C. (2009), Drought sucks life from Argentinas farms, http://news.bbc.co.uk/2/hi/americas/7905357.stm, accessed on 2011 March 3.

Rüdiger, C., T. Holmes, J.-C. Calvet, R. de Jeu, and W. Wagner (2009), An intercomparision of ERS-Scat, AMSR-E and SVAT soil moisture observations over France, *Journal of Hydrometeorology*, **10**(2), p. 431, doi:10.1175/2008JHM997.1.

Ross, D., and W. L. Jones (1978), On the relationship of radar backscatter to wind speed and fetch, *Boundary-Layer Meteorology*, **13**, p. 151–163.

Scipal, K. (2002), Global Soil Moisture Retrieval from ERS Scatterometer Data, Ph.D. thesis, Vienna University of Technology, Austria.

Stark, J. (2005), *Product lifecycle management : 21st century paradigm for product realisation*, Springer, London.

Stoffelen, A. C. M. (1998), Scatterometry, Ph.D. thesis, Universiteit Utrecht, The Netherlands.

Sunda, M., R. Crapolicchio, and P. Lecomte (2002), Impact of satellite degraded attitude on ERS-2 Scatterometer data, in *Proceedings of SPIE, Remote Sensing of the Ocean and Sea Ice*, Agia Pelagia, Greece, 23-27 September 2002.

Tsai, W.-T., M. Spencer, C. Wu, C. Winn, and K. Kellogg (2000), SeaWinds on QuikSCAT: sensor description and mission overview, in *IEEE International Geoscience and Remote Sensing Symposium (IGARSS)*, p. 1021–1023, Honolulu, Hawaii, USA, 24-28 July.

Ulaby, F. T., R. K. Moore, and A. K. Fung (1981), *Microwave Remote Sensing: Active and Passive. Vol. I – Microwave Remote Sensing Fundamentals and Radiometry*, Addison-Wesley, Advanced Book Program, Reading, MA, USA.

Ulaby, F. T., R. K. Moore, and A. K. Fung (1982), *Microwave Remote Sensing: Active and Passive. Vol. II – Radar Remote Sensing and Surface Scattering and Emission Theory*, Addison-Wesley, Advanced Book Program, Reading, MA, USA.

Wagner, W. (1998), Soil Moisture Retrieval from ERS Scatterometer Data, Ph.D. thesis, Vienna University of Technology, Austria.

Wagner, W. (2005), Implementation Plan for a Soil Moisture Product for NWP, ASCAT Soil Moisture Report Series, No. 5, *Technical Report*, Institute of Photogrammetry and Remote Sensing, Vienna University of Technology, Austria.

Wagner, W., G. Lemoine, and H. Rott (1999a), A method for estimating soil moisture from ERS scatterometer and soil data, *Remote Sensing of Environment*, **70**(2), p. 191–207.

Wagner, W., J. Noll, M. Borgeaud, and H. Rott (1999b), Monitoring soil moisture over the Canadian Prairies with the ERS scatterometer, *IEEE Transactions on Geoscience and Remote Sensing*, **37**, p. 206–216.

Wagner, W., K. Scipal, C. Pathe, D. Gerten, W. Lucht, and B. Rudolf (2003), Evaluation of the agreement between the first global remotely sensed soil moisture data with model and precipitation data, *Journal of Geophysical Research D: Atmospheres*, **108**(D19), p. Art. No. 4611.

Wertz, J., and W. Larson (1999), *Space mission analysis and design*, Space technology library, 3rd ed., Microcosm.

Wilson, J. J. W., P. L. Phillips, J. Figa-Saldaña, K. Dumper, and T. Fiksel (2005), Radiometric calibration of the advanced wind scatterometers carried on-board the METOP satellites, in *IEEE International Geoscience and Remote Sensing Symposium (IGARSS)*, p. 3436–3440, Seoul, South Korea, 25–29 July.

Wilson, J. J. W., C. Anderson, M. A. Baker, H. Bonekamp, J. Figa-Saldaña, R. G. Dyer, J. A. Lerch, G. Kayal, R. V. Gelsthorpe, M. A. Brown, E. Schied, S. Schutz-Munz, F. Rostan, E. W. Pritchard, N. G. Wright, D. King, and . Önel (2009), Radiometric Calibration of the Advanced Wind Scatterometer Radar ASCAT carried on-board the METOP-A Satellite, *IEEE Transactions on Geoscience and Remote Sensing*, p. in press.

Woodhouse, I. H. (2006), *Introduction to Microwave Remote Sensing*, CRC Press, Boca Raton, FL, USA.